Journal Pre-proof

Ultrastructure, composition, and $^{87}Sr/^{86}Sr$ dating of shark teeth from lower miocene sediments of southwestern Peru

Giulia Bosio, Giovanni Bianucci, Alberto Collareta, Walter Landini, Mario Urbina, Claudio Di Celma

PII: S0895-9811(22)00198-5

DOI: https://doi.org/10.1016/j.jsames.2022.103909

Reference: SAMES 103909

To appear in: *Journal of South American Earth Sciences*

Received Date: 28 March 2022

Revised Date: 27 June 2022

Accepted Date: 27 June 2022

Please cite this article as: Bosio, G., Bianucci, G., Collareta, A., Landini, W., Urbina, M., Di Celma, C., Ultrastructure, composition, and $^{87}Sr/^{86}Sr$ dating of shark teeth from lower miocene sediments of southwestern Peru, *Journal of South American Earth Sciences* (2022), doi: https://doi.org/10.1016/j.jsames.2022.103909.

Ultrastructure, composition, and $^{87}Sr/^{86}Sr$ dating of shark teeth from lower Miocene sediments of southwestern Peru

Giulia Bosio[1]*, Giovanni Bianucci[2], Alberto Collareta[2], Walter Landini[2], Mario Urbina[3], Claudio Di Celma[4]

[1] Dipartimento di Scienze dell'Ambiente e della Terra, Università degli Studi di Milano-Bicocca, 20126 Milano, Italy

[2] Dipartimento di Scienze della Terra, Università di Pisa, 56126 Pisa, Italy

[3] Departamento de Paleontología de Vertebrados, Museo de Historia Natural, Universidad Nacional Mayor de San Marcos, Lima 1, Peru

[4] Scuola di Scienze e Tecnologie, Università di Camerino, 62032 Camerino, Italy

* *Corresponding author. E-mail address: giulia.bosio.giulia@gmail.com*

Highlights

- Enameloid of fossil shark teeth is more resistant to alteration than dentine
- We achieve ultrastructural and compositional data on Miocene Peruvian shark teeth
- Good preservation of the enameloid allows for successful Sr isotope dating
- $^{87}Sr/^{86}Sr$ values date the Chilcatay strata to the Burdigalian in the Ica River Valley
- Chilcatay strata at Media Luna are dated for the first time to ca. 22–20 Ma

Abstract

Bioapatite of fossil bone and teeth is susceptible to alteration and ion exchange during burial and diagenesis, varying its Sr content through the geological time. Nevertheless, fossil shark teeth are a powerful proxy for both chronostratigraphic and paleoecological reconstructions, thanks to the

presence of the enameloid, a hard outer layer consisting of resistant fluorapatite crystallites. Here, we analyze fossil shark teeth from the Miocene sediments of the Chilcatay Formation in the Pisco Basin (southwestern Peru) with the aim of dating poorly constrained strata in this region. (Ultra)structural and compositional analyses on fossil lamniform and carcharhiniform teeth are performed through macroscopical observations, optical microscopy and SEM-EDS for evaluating the preservation state of the collected teeth. Shark teeth display a compact and well preserved outer enameloid layer formed by highly ordered bundles of crystallites that is distinctly separated by a more porous and heterogeneous inner core of dentine featuring diagenetic artefacts and microborings. Compositional mapping highlights differences in distribution of Ca, P, F, and S in the enameloid and dentine, and chemical results show a Sr content that is consistent with the range reported for extant shark teeth. The best preserved teeth were selected for Strontium Isotope Stratigraphy (SIS), measuring the $^{87}Sr/^{86}Sr$ values in the enameloid and obtaining numerical (absolute) age estimates. At the Ica River Valley, SIS dates the Chilcatay strata to the Burdigalian (between 19.1 and 18.1 Ma), in agreement with previous radiometric, isotopic and biostratigraphic ages obtained in the same region. At Media Luna, the Chilcatay strata are dated herein for the first time, resulting in a slightly older age of 21.8–20.1 Ma (late Aquitanian–early Burdigalian). These results strengthen the notion that the Sr-ratio of shark teeth can be successfully applied for obtaining reliable age estimates via SIS.

Keywords

Strontium Isotope Stratigraphy (SIS), enameloid, dentine, bioapatite, Pisco Basin, Chilcatay Formation

1. Introduction

Fossil bones and teeth can resist through geological time thanks to their mineralized calcium phosphate composition. Vertebrate teeth are formed by hydroxyapatite with some carbonate

substitutions in phosphate positions (Francillon-Vieillot et al., 1990; Dahm and Risnes, 1999). In contrast to mammalian teeth, where the mineralized matrix is largely hydroxyapatite (Francillon-Vieillot et al., 1990), shark teeth contain fluorapatite, $Ca_5(PO_4)F$, as biomineral phase with partial substitution of phosphate by carbonate or substitution of fluoride by hydroxide (Møller et al., 1975; Daculsi and Kerebel, 1980). This unique feature makes shark teeth remarkably resistant, as fluorapatite is the least soluble form of apatite and more resistant to alteration than other phosphate phases (Posner et al., 1984; Gardner et al., 1992; Brunet et al., 1999). In particular, modern shark teeth are composed of fluorapatite only in the enameloid outer portion (Lübke et al., 2015), whereas the dentine is made of fluorohydroxyapatite, $Ca_5(PO_4)_3(OH, F)$. Enameloid is a kind of tooth coating exclusive of many fishes including sharks, whereas mammalian teeth are coated by enamel (Peyer, 1968; Carlson, 1990; Cappetta, 2012; Cuny et al., 2017). Enamel and enameloid are more coarsely crystalline and have a lower organic matter content compared to dentine, which is more finely grained and contains higher contents of water, organic matter, and carbonate (Carlson, 1990; Enax et al., 2012). Enameloid is also six times harder than dentine, and displays a highly ordered structure (Enax et al., 2012, 2014); it constitutes the outer layer that covers the crown of the tooth, whereas dentine forms the inner part of the crown and the root (Cappetta, 2012, and references therein).

As regards tooth histology, two main histotypes are recognized: the orthodont histotype and the osteodont hystotype (Glickman, 1967; Compagno, 1988; Cappetta, 2012) (Fig. 1). According to the original definition, orthodont teeth retain an open pulp cavity throughout the tooth development, whereas osteodont teeth have their pulp cavity gradually filled by osteodentine (Ørvig, 1951) as development proceeds (Thomasset, 1930; Moyer et al., 2015). Orthodont teeth feature orthodentine (Peyer, 1968) that encapsulates the pulp cavity, whereas osteodentine forms the root; osteodont teeth, in turn, lack orthodentine and are completely filled by osteodentine that also forms the root (Moyer et al., 2015). More recently, a third tooth type has been identified, i.e. the pseudoosteodont histotype, in which the pulp cavity is secondarily replaced by osteodentine (Jambura et al., 2018;

2020). In light of this subdivision, the two galeomorph shark orders Lamniformes and Carcharhiniformes (with the exception of *Hemipristis*) represent the two histotype end-members, i.e. osteodont and orthodont, respectively (Moyer et al., 2015; Schnetz et al. 2016) (Fig. 1). Indeed, the osteodont histotype is exclusive of lamniforms, showing a unique histological pattern that reflects a phylogenetic signal (Jambura et al., 2020).

The outer enameloid layer is formed by highly ordered bundles of fluorapatite crystallites with a roughly hexagonal section (Daculsi and Kerebel, 1980; Chen et al., 2014; Enax et al., 2014; Lübke et al., 2015; Wilmers et al., 2021). It is organized in a triple layered structure (Reif, 1973; Cuny and Risnes 2005 and references therein): the Shiny-Layered Enameloid (SLE), which is also compositionally distinctive (Enax et al., 2014), the Parallel-Bundled Enameloid (PBE), and the Tangled-Bundled Enameloid (TBE) (Cuny et al., 2001). The PBE and TBE correspond to the Parallel-Fibered Enameloid (PFE) and the Tangle-Fibered Enameloid (TFE) of Reif (1973) and Moyer et al. (2015) (Fig. 5C-F). Recently, these layers have been grouped into two distinct units: an external one, i.e. the Single Crystallite Enameloid (SCE) or Ridge/Cutting Edge Layer + Shiny-Layered Enameloid (RCEL+SLE), and an internal bundled one, i.e. the Bundled Crystallite Enameloid (BCE), the latter including both the PBE and TBE (Cuny and Risnes 2005; Botella et al., 2009; Guinot and Cappetta, 2011; Enault et al., 2015).

On the other hand, the dentine is a porous tissue with a high organic matter content and vascular canals. Dentine is also easily recognizable from enameloid by virtue of its disordered crystals (Lübke et al., 2015) and a different chemical composition (Enax et al., 2014). Several types of vertebrate dentine have been described, among which are osteodentine and orthodentine. Osteodentine has a bone-like appearance and is made up of dentinal osteons and interosteonal tissue (Radinsky, 1961). A dentinal osteon consists of a vascular canal surrounded by concentric lamellae of circumvascular dentine, that are penetrated by dentinal tubules, whereas the tissue among dentinal osteons is known as the interosteonal tissue (Radinsky, 1961). Orthodentine has been

104 described as a tissue comprise of circumpulpar and pallial dentine exhibiting parallel and branching
105 tubules (Radinsky, 1961; Smith and Sansom, 2000).

106 Due to the resistance to alteration of shark teeth, geochemical and isotopic studies are often
107 carried out on fossil shark teeth (e.g., Schmitz et al., 1997; Tütken et al., 2011; Akhtar et al., 2020)
108 for paleoecological and paleoenvironmental reconstructions and, less frequently, for
109 geochronological applications like Strontium Isotope Stratigraphy (SIS) (John et al., 2013).

110 First conceived by Wickman (1948), the SIS method is based on the assumption that strontium
111 has a roughly uniform global distribution in the global ocean due to its long residence in seawater
112 (ca. 10^6 years), which is much higher than the average mixing time of seawater in the oceans (ca.
113 10^3 years) (McArthur et al., 2020). The Sr ratio has varied through the geological time due to the
114 variable silicate riverine input and hydrothermal circulation at mid-ocean ridges; thus, the Sr values
115 can be linked to a precise geological age (Peterman et al., 1970; McArthur, 1994; Veizer et al.,
116 1997; Peucker-Ehrenbrink and Fiske, 2019; McArthur et al., 2020). In order to obtain the best-fit
117 curve from the $^{87}Sr/^{86}Sr$ data (Burke et al., 1982), a LOESS fit, deriving from the LOWESS
118 statistical method (Cleveland, 1981), has been elaborated through calibration with the GTS2020
119 Timescale (McArthur et al., 2020).

120 Marine authigenic minerals can preserve the $^{87}Sr/^{86}Sr$ ratio of the seawater in which they
121 precipitate (Veizer, 1989). Strontium is incorporated in calcium carbonate and calcium phosphate
122 crystals by substituting calcium; this is made possible by the similar ionic radius and oxidation state
123 of Sr and Ca (Faure and Mensing, 2005). For this reason, marine authigenic minerals such as
124 carbonates comprise excellent tools for dating and correlating sedimentary successions, provided
125 that they have not undergone diagenetic alteration (e.g., DePaolo and Ingram, 1985). As other
126 marine authigenic minerals, phosphates - and in particular bioapatite – can be used for $^{87}Sr/^{86}Sr$
127 stratigraphic dating (Staudigel et al., 1985). Thus, the SIS has been successfully applied to fossil
128 bones and teeth from marine deposits, despite the porous structure of the bony tissues (which makes
129 them susceptible to diagenetic alteration) and the sparse fossil record of marine vertebrates (John et

al., 2013). Fossil bones and teeth can incorporate diagenetic Sr in different ways: i) via pore-filling by secondary minerals; ii) by recrystallization of hydroxyapatite; iii) through direct exchange in the original hydroxyapatite crystals; and iv) by absorption in microcracks or on the surfaces of hydroxyapatite crystals (Hoppe et al., 2003). For this reason, a diagenetic screening is always needed before proceeding with Sr ratio analyses. Shark teeth are particularly suitable for SIS. They are resistant to diagenesis due to their fluorapatite composition (LeGeros, 1990; Gardner et al., 1992; Brunet et al., 1999) and are relatively abundant in the fossil record due to their cyclical replacement during lifetime (Kemp, 1999; Tucker and Fraser, 2014). In addition, Vennemann et al. (2001) demonstrated that the $^{87}Sr/^{86}Sr$ ratios of modern shark teeth reflect uniform present-day seawater values. However, Grandjean and Alberède (1989) and Kohn et al. (1999) described three modes of alteration of the fossil tooth composition: i) by diagenetic formation of Fe and Mn oxyhydroxides (resulting in higher Fe, Mn, Ba and Cu contents); ii) trapping of silicate particles of terrigenous origin (resulting in higher Al and Si contents); and iii) chemical change of bioapatite due to recrystallization (resulting in higher U and Sr content) (John et al., 2013). In order to exclude any compositional alteration, a comparison with the chemical composition of modern shark teeth should be carried out before analyzing fossil specimens for SIS (John et al., 2013; Hättig et al., 2019).

Although Barrat et al. (2000) and Martin and Scher (2004) assessed that the Sr isotopic values of fish teeth may be altered during and after burial through exchange with pore fluid Sr^{2+}, $^{87}Sr/^{86}Sr$ dating on shark teeth has provided reliable age estimates in several cases (Vennemann and Hegner, 1998; Becker et al., 2008; Harrel et al., 2016; Tütken et al., 2020). In particular, Sr isotope measurements of the enameloid layer give Sr ages that are more reliable than observed for dentine (Becker et al., 2008; Tütken et al., 2020). This is due to the resistance of enameloid to diagenetic processes and weathering (Roelofs et al., 2017), similar to the enamel of mammalian teeth (Ayliffe et al., 1994; Kohn et al., 1999; Zazzo et al., 2004; Tütken et al., 2008). Dentine is therefore more prone to recrystallize during diagenesis than enameloid and other hypermineralized tissues that are

more resistant to diagenetic alteration (Roelofs et al., 2017). However, it must be pointed out that the application of SIS on shark teeth from the Cenozoic successions comports some limitations as concerns the Paleogene, due to the oscillation and flattening of the calibration curve in correspondence of this system/period (McArthur et al., 2020).

In order to test the feasibility of SIS in the shark tooth-rich sediments of the Pisco Basin (Peru), and aiming to date some poorly-constrained strata exposed at various Ica River Valley localities, we analyzed the ultrastructure, composition and $^{87}Sr/^{86}Sr$ ratios of fossil shark teeth from the Chilcatay Formation. The Miocene marine sediments of this sedimentary unit host an abundant fossil content of marine vertebrates (Bianucci et al., 2015, 2018a, b, 2020; Lambert et al., 2015, 2018, 2020, 2021; Di Celma et al., 2018, 2019; Collareta, 2021b; Bianucci and Collareta, 2022), among which elasmobranch remains are present and locally common (Bianucci et al., 2018b; Di Celma et al., 2019; Landini et al., 2019). Here, we present the first attempt to date the shark teeth from the Chilcatay Formation by means of SIS. Teeth of *Cosmopolitodus hastalis*, *Isurus oxyrinchus*, *Isurus* sp., *Megalolamna paradoxodon* and *Physogaleus contortus* were analyzed from the Chilcatay strata at the localities of Zamaca, Media Luna and near Cerro Colorado, deciphering also their diagenetic imprints.

2. Geological and paleontological framework

2.1. Tectonic and stratigraphic setting

The Peruvian forearc system formed in response to the mid-Eocene-to-Recent westward subduction of the Farallon-Nazca Plate beneath the South America Plate and consists of elongated trench-parallel sedimentary basins separated by tectonically active structural ridges, i.e. the Outer Shelf High and the Upper Slope Ridge (Travis et al., 1976; Thornburg and Kulm, 1981; Klein et al., 2011, and references therein). One of these basins is the Pisco Basin, which is divided into the West Pisco Basin and the East Pisco Basin by the Coastal Cordillera, the onshore prolongation of the Outer Shelf High (Romero et al., 2013). The East Pisco Basin, a 180-km-long depression extending

between the towns of Pisco and Nazca, has been active between the Eocene and the Pliocene with the deposition of marine sedimentary units (Dunbar et al., 1990; DeVries, 1998) (Fig. 2A, B). The latter are, from oldest to youngest, the Caballas Formation, the Paracas Formation, the Otuma Formation, the Chilcatay Formation and the Pisco Formation (DeVries, 2017; DeVries et al., 2017; DeVries and Jud, 2018; Di Celma et al., 2017, 2018a, 2019, in press). Since the latest Pliocene, regional uplift occurred, being caused by the subduction of the Nazca Ridge, which impinged the overlying South American plate at 11°S latitude approximately 11.2 Ma and generated the volcanic gap that is currently observed in most of the Peruvian Andes (Hsu, 1992; Macharé and Ortlieb ,1992; von Huene et al., 1996; Hampel, 2002; Klein et al., 2011). Due to this uplift, nowadays most of the basin is exhumed and its sedimentary succession is exposed in the Ica Desert.

Sediments of the Chilcatay Formation deposited during the latest Oligocene and early Miocene in a semi-enclosed , shallow-marine embayment studded with several basement islands (Marocco and Muizon, 1988b; DeVries and Jud, 2018; Bianucci et al., 2018b). In the Ica River Valley, two different depositional sequences can be recognized in the Chilcatay Formation, namely, Ct1 and Ct2, separated by the CE0.2 intraformational unconformity (Di Celma et al., 2018b, 2019) (Fig. 2B). Both sequences are marked at the base by a basal lag with boulders, pebbles marked by *Gastrochaenolites* borings, phosphatic nodules, shark teeth, oysters, and bone fragments, as well as by large, passively infilled *Thalassinoides* and *Gyrolithes* burrows. The Ct1 sequence includes three facies associations, recording shoreface, offshore and submarine delta deposition: massive sandstones with boulder-sized clasts and conglomerates (*Ct1c*), sandstones and siltstones intercalated by beds of coarse-grained sandstones and conglomerate beds (*Ct1a*), and coarse-grained mixed siliciclastic-carbonate clinobedded deposits (*Ct1b*). The Ct2 sequence consists of two facies associations, recording shoreface and offshore deposition: highly fossiliferous, massive and intensely bioturbated sandstones (*Ct2a*), and silty mudstone intercalated with minor, laterally persistent, very fine-grained sandstone interbeds as well as submarine slump-related contorted strata (*Ct2b*). In the southern part of the Ica River Valley, at the locality of Laberinto, an older

unconformity-bounded unit has been recognized by DeVries et al. (2021) and designated therein as Chilcatay-0 or Ct0.

The Chilcatay Formation has been assigned to the upper Oligocene–lower Miocene in the East Pisco Basin and surroundings (Dunbar et al., 1990; DeVries, 1998; DeVries and Jud, 2018). At the Ica River Valley localities of Ullujaya and Roca Negra, the Chilcatay Formation has been lately dated to the Burdigalian via the integration of micropaleontological biostratigraphy and isotope geochronology (Di Celma et al., 2018b; Lambert et al., 2018; Bosio et al., 2020a, b). At Laberinto, in turn, the Chilcatay-0 (Ct0) strata span chronostratigraphically between ca. 21 Ma and 20 Ma (DeVries et al., 2021). Biostratigraphic data based on silicoflagellates, diatoms and nannoplankton constrain the deposition of the Ct1 and Ct2 strata between ca. 19 Ma and 18 Ma. This age range is confirmed by $^{40}Ar/^{39}Ar$ ages obtained from two volcanic ash layers from the Ct1 sequence, dated at 19.25 ± 0.05 Ma (at the base of the Chilcatay succession at Roca Negra) and 19.00 ± 0.28 Ma (at Ullujaya), as well as one volcanic ash layer found near the top of Ct2, dated at 18.02 ± 0.07 Ma (at Los Dos Cerritos) (Fig. 2B). In addition, the $^{40}Ar/^{39}Ar$ dating of an ash layer from undifferentiated Chilcatay near the type locality of *Macrosqualodelphis ukupachai* (an unnamed site south of Cerro Colorado) gives an age 18.78 ± 0.08 Ma (Bianucci et al., 2018a). At the aforementioned sites of Roca Negra and Ullujaya, $^{87}Sr/^{86}Sr$ datings on well preserved carbonates (oysters, pectinids and barnacles) from the Ct1 sequence give concordant ages of 18.85–18.00 Ma, obtained with the LOWESS 5 Table calibrated to the GTS2012 Timescale (Bosio et al., 2020a).

2.2. Paleontological setting

The Pisco Basin is renowned for hosting a very outstanding marine vertebrate Fossil-Lagerstätten (e.g., Colbert, 1944; Marocco and Muizon, 1988a; Muizon, 1988; Brand et al., 2004, 2011; Esperante et al., 2008, 2015; Uhen et al., 2010; Bianucci et al., 2015, 2018a, b, 2020; Lambert et al., 2015, 2018, 2020, 2021; Stucchi et al., 2016; Di Celma et al., 2018, 2019; Boskovic et al., 2021; Bosio et al., 2021b; Collareta, 2021b; Bianucci and Collareta, 2022), but also for

remarkable finds of fossil invertebrates (e.g., Alleman, 1978; DeVries, 1988; DeVries and Frassinetti, 2003; Bosio et al., 2021a; Kočí et al., 2021; Sanfilippo et al., 2021) as well as for microfossil studies (e.g., Mertz, 1966; Macharé and Fourtanier, 1987; Schrader and Ronning, 1988; Marty, 1989; Tsuchi et al., 1988; Koizumi, 1992; Ibaraki, 1993; Gariboldi, 2016; Coletti et al., 2019a; Malinverno et al., 2021). As regards the fossil invertebrates, the Chilcatay Formation features an abundant and rather diverse fauna comprised of mollusks, acorn barnacles, cirratulids, echinids, brachyuran decapods, and rare bryozoans and benthic foraminifera (Coletti et al., 2018; Di Celma et al., 2018b). Mollusks dominate the assemblage, with abundant oysters, pectinids and gastropods; among them, DeVries and Jud (2018) recognized *Ficus distans*, *Turritella cruzadoi*, *Olivancellaria tumorifera*, *Tilicrassatella ponderosa* and *Glycymeris ibari* as index molluscan species for the Chilcatay Formation. Specimens of *Acanthina katzi*, *Testallium cepa*, *Misifulgur cruziana*, and *Turritella woodsi* are also found in the Chilcatay strata, together with *Chlamys* and less common representatives of *Miltha*, *Conus*, *Crepidula*, *Panopea*, *Olivella*, *Sinum* and *Calyptrea* (*Trochita*). Among gastropods, the vermetid *Thylacodes devriesi* is common in the assemblage as a reef-forming species (Sanfilippo et al., 2021). The brachiopod genus *Discinisca* is also present (DeVries and Jud, 2018). Barnacles are also abundant and dominate the assemblage in two different facies (Coletti et al., 2018). At least three different species of balanid barnacles are present in the Chilcatay Formation, including *Austromegabalanus carrioli* and *Perumegabalanus calziai* (Collareta et al., 2019; Coletti et al., 2019b). Finally, cirratulid reefs of the species *Diplochaetetes mexicanus* are present in the Chilcatay strata (Kočí et al., 2021).

Fossil vertebrates from the Chilcatay Formation are mostly known from the localities of Cerro Colorado, Santa Rosa, Ullujaya and Zamaca, and include cetaceans, seabirds, marine reptiles and fishes (teleosts as well as sharks and rays). Cetaceans are mostly represented by odontocetes (echolocating toothed whales) belonging to the enigmatic heterodont inticetids (*Inticetus vertizi*), the so-called "*Chilcacetus*-clade" of archaic homodont odontocetes (*Chilcacetus cavirhinus*), the platanistoids (relatives of the South Asian river dolphins, namely, the squalodelphinids *Furcacetus*

flexirostrum, *Huaridelphis raimondii*, *Macrosqualodelphis ukupachai* and *Notocetus vanbenedeni*, the platanistid aff. *Araeodelphis* sp., the basal platanistoid *Ensidelphis riveroi*, and other indeterminate forms), the eurhinodelphinids (long-snouted relatives of the present-day beaked whales, represented by indeterminate specimens only), the physeteroids (sperm whales, including cf. *Diaphorocetus* sp. and *Rhaphicetus valenciae*), and the early branching delphinidan genus *Kentriodon* (Lambert et al., 2014, 2015, 2020, 2021; Bianucci et al., 2015, 2018a, b, 2020; Di Celma et al., 2018, 2019; Bosio et al., 2021b; Bianucci and Collareta, 2022). Mysticetes (baleen-bearing whales) are also present but rare and poorly known (Di Celma et al., 2019). Seabirds are represented by the extinct slender-footed penguin *Palaeospheniscus* (Acosta-Hospitalache and Stucchi, 2005). Marine reptiles consist of at least one dermochelyid (leatherback turtle) taxon possibly corresponding to *Natemys peruvianus* (Wood et al., 1996; Bianucci et al., 2018b; Di Celma et al., 2019). Bony fishes include indeterminate tuna-like forms besides billfish (aff. *Makaira* sp.) and abundant cycloid scales that recall the extant pilchard genus *Sardinops* (Bianucci et al., 2018b; Di Celma et al., 2018b, 2019).

Elasmobranch remains are abundant in the Chilcatay strata and concentrate in a few discrete stratigraphic intervals (Di Celma et al., 2018; Bianucci et al., 2018b; Landini et al., 2019), though sometimes shark teeth are found associated with cetacean skeletons, possibly suggesting scavenging action (Bianucci et al., 2018a; Lambert et al., 2018). Some information on the lower Miocene elasmobranch remains collected along the western bank of the Ica River was reported by Alván De la Cruz (2008), Renz (2009) and Shimada et al. (2019), but a more comprehensive overview of the shark and ray assemblage from the Chilcatay strata was only presented by Bianucci et al. (2018b) and Landini et al. (2019). From the nearby localities of Ullujaya and Zamaca, these authors listed teeth and dermal elements belonging to Squatiniformes (angel sharks, *Squatina* sp.), Lamniformes (mackerel sharks, including *Alopias superciliosus*, *Alopias* cf. *vulpinus*, *Anotodus agassizi*, *Cosmopolitodus hastalis*, *Cosmopolitodus plicatilis*, *Isurus oxyrinchus*, *Megachasma* cf. *applegatei*, *Carcharias* sp., *Carcharocles chubutensis*, *Megalolamna paradoxodon* and *Parotodus benedeni*),

Carcharhiniformes (ground sharks, including *Carcharhinus brachyurus*, *Carcharhinus* cf. *leucas*, *Galeocerdo aduncus*, *Negaprion brevirostris*, *Physogaleus contortus*, *Hemipristis serra* and *Sphyrna zygaena*), Myliobatiformes (stingrays and relatives, including Dasyatidae gen. et sp. indet. and Myliobatoidea gen. et sp. indet.) and Rhinopristiformes (sawfishes and relatives, only represented by *Anoxypristis* sp.). The structure of the Ullujaya and Zamaca assemblages is mainly described by three key features: 1) a taxonomic composition dominated by two shark lineages, Lamniformes and Carcharhiniformes, the former being dominant in terms of alpha-diversity; 2) the leading role played by two species, *C. brachyurus* and *C. hastalis*, accounting for more than three fifths of the studied specimens; 3) the distinctly juvenile imprint of the entire assemblage. Striking similarities were noted by Landini et al. (2019) between the elasmobranch assemblage from Zamaca and that from the upper Miocene Pisco strata exposed at Cerro Colorado (Landini et al., 2017a, b), thus suggesting the persistence of a peculiar "biological enclave" driven by the concurrence of the ecological, environmental, and oceanographic factors that characterized the coast of present-day Peru throughout the Miocene (Collareta et al., 2021b).

3. Material and Methods

3.1. Study area and sample collection

Fossil tooth samples were collected in the Ica Desert near the village of Ocucaje, along the western side of the Ica River Valley, at four localities where the Chilcatay Formation crops out (Fig. 2A). The first two localities take their place ca. 3-4 km south of Cerro Colorado, where shark teeth occur in association with two important cetacean specimens from undifferentiated Chilcatay strata: an undescribed new genus and species of eurhinodelphinid-like odontocete (14°23'46.8'' S, 75°53'15.8'' W) (Fig. 3E) and the holotype of *Macrosqualodelphis ukupachai* (14°23'01.9'' S, 75°53'58.8'' W) (MUSM 2545, Bianucci et al., 2018a). Since the Chilcatay Formation is not mapped in detail nor chronostratigraphically constrained in this area, shark teeth were collected from close to both cetacean skeletons for chronostratigraphic purposes. In addition, oyster

specimens were collected from the same stratigraphic layer as MUSM 2545. Another studied locality is placed in the Zamaca area (Fig. 2), where the Chilcatay Formation is widely exposed (Di Celma et al., 2019). Here, shark teeth were sampled from the shark tooth-bearing bed ShB-4 occurring at the base of the Ct2 sequence (Landini et al., 2019) (Fig. 3A–D). The fourth investigated locality is Media Luna, a coastal site 25 km west of the Ica River (Fig. 2). In this locality, the Chilcatay Formation is still undated, and two different shark tooth-bearing horizons have recently been identified and are still under study. Shark teeth were sampled from the lower horizon, "Terrace 1" for chronostratigraphic and paleoecological purposes (Fig. 3F).

3.2. Laboratory analyses

The collected shark teeth were first analyzed macroscopically for evaluating the preservation state and screened for diagenetic alteration. The completeness of the root, color, crown preservation and presence/absence of weathering wear were taken into account for selecting the sixteen best preserved specimens suitable for further analyses. Fossil shark teeth belonging to the families Lamnidae, Otodontidae and Charcharinidae (Fig. 4) were analyzed in depth macroscopically, petrographically and compositionally. Five polished thin sections covering all the aforementioned localities and families were prepared at the laboratories of TS Lab & Geoservices in Pisa, embedding the teeth in epoxy resin and cutting them along the coronal plane. Two additional thin sections from oyster samples were also realized. Petrographic analyses were carried out through a Leica optical microscope at the Università degli Studi di Milano-Bicocca for investigations on dental internal structure and searching evidence of alteration and/or diagenesis.

Scanning Electron Microscopy (SEM) and Energy-Dispersive X-ray Spectroscopy (EDS) were performed through a Zeiss FEG Gemini 500 at the Università degli Studi di Milano-Bicocca. Secondary Electron (SE) images were achieved for describing the ultrastructure of the enameloid, dentine and dentine-enameloid junction. Backscattered electron (BSE) images and compositional

maps of major elements were realized in order to determine the chemical composition of enameloid and dentine and their dissimilarities.

Based on these preliminary analyses, eleven shark teeth and two oyster samples were chosen for applying the SIS (Table 1). The selected specimens were immersed in distilled water and cleaned in an ultrasonic bath for removing any remaining sediment particle. After drying, pristine oyster layers were drilled with a Dremel micro-drill to obtain shell powder from the unaltered portions. Shark teeth were simply scraped at the surface with a Dremel micro-drill for removing a small amount of enameloid from the tooth crown, avoiding dentine. An amount of ca. 8–30 mg of powder was collected from each sample avoiding contaminations, and sent at the Ruhr-Universität Bochum, where Inductively Coupled Plasma-Optical Emission Spectroscopy (ICP-OES) and $^{87}Sr/^{86}Sr$ analyses were carried out.

ICP-OES analyses were performed through a Thermo Fisher Scientific iCAP 6500 DUO spectrometer for measuring Sr, Ca, Mg, Fe and Mn concentrations. A TI-Box (Spectromat) Thermal Ionisation Mass Spectrometer (TIMS) with seven collectors was employed for determining $^{87}Sr/^{86}Sr$ ratios, using a dynamic (peak-hopping) mode of measurement. The cut-off limit for a strontium run was an error of $\pm 2\sigma \leq 5 \times 10^{-6}$ for the $^{87}Sr/^{86}Sr$ ratio, with 100–200 ratios per run (typical duration: 110 ratios, lasting 2 h and 15 min, plus the filament heating time). The standards NIST NBS 987 and USGS EN-1 were employed in the analyses, with a long-term mean measured at Bochum of 0.710246 ± 0.000027 (2σ) and 0.709163 ± 0.000037 (2σ), respectively. No Rb (rubidium) correction was applied, but Rb abundances were nonetheless monitored during the entire run. When Rb levels exceeded the detection limit, the result was discarded and the measurement repeated.

$^{87}Sr/^{86}Sr$ results were corrected for the difference between the USGS EN-1 value used for the compilation of McArthur's reference curve and the USGS EN-1 Bochum mean value. $^{87}Sr/^{86}Sr$ corrected values were converted into ages using the LOESS Table 6 calibrated to the GTS2020 Timescale (McArthur et al., 2020). For estimating the age of a single stratigraphic layer from several analyzed samples, a mean $^{87}Sr/^{86}Sr$ value was calculated and then converted to age (Frijia et

al., 2015). The uncertainty for each stratigraphic level was calculated as 2 standard errors (2 s.e.) from the standard deviation of the mean. For both single samples and stratigraphic layers, a maximum age, a preferred age and a minimum age were obtained.

4. Results

4.1. Shark tooth preservation

The collected shark teeth belong to the families Lamnidae, Otodontidae (Lamniformes), and Carcharinidae (Carchariniformes) (Fig. 4). All the fossil teeth are moderately well to well preserved, and no evident wear, bioerosion or encrusters were detected. Specimens from both the localities south of Cerro Colorado display almost intact tooth roots and crowns. The latter are homogeneously capped by enameloid, which in few cases exhibits very thin fracture lines (Fig. 4). The selected teeth collected near the eurhinodelphinid-like odontocete skeleton mostly belong to Lamnidae, including two teeth of *Cosmopolitodus hastalis* and one of *Isurus oxyrinchus*; one further tooth belongs to *Physogaleus contortus*, the only carcharhinid analyzed in this study. The two selected teeth collected in association with the *Macrosqualodelphis ukupachai* holotype belong to the lamnid species *C. hastalis*. In addition, two oysters were also selected from the same site for conducting further analyses thanks to their well preserved visible layers of unaltered nacre.

At Zamaca, the shark tooth-bearing basal interval of the Ct2 sequence (Landini et al., 2019) is composed of sandstones showing sub-rounded to sub-angular pebbles derived from the immediately underlying siltstones, basement clasts, rare coal fragments, dispersed crustaceans (crabs and barnacles), and shark teeth and vertebrae (Fig. 3). Teeth from the ShB-4 bed range from moderately to well preserved, displaying an almost intact root and a crown coated by an intact layer of enameloid. Many teeth also feature a brownish color (Fig. 3D) that is probably due to phosphatization, and were thus discarded from further analyses. Three well preserved lamnid teeth, belonging to *C. hastalis* and *I. oxyrinchus* were selected for further analyses.

388 At the Media Luna locality, the stratigraphic lowest shark tooth-bearing horizon is
389 characterized by coarse-grained sediment enriched in shark teeth. Shark fossils are still under study
390 and include some deep-water elements (e.g., *Pristiophorus*) that contrast with the shallow-water,
391 marginal-marine assemblage retrieved at Zamaca (Landini et al., 2019). Further contrasting with the
392 condition observed at Zamaca and south of Cerro Colorado, in the Media Luna beds, shark teeth
393 almost invariably lack their roots and often exhibit a loss of the internal dentine filling. Only very
394 few teeth have a moderately well preserved root and an intact crown. Among the latter, four teeth of
395 *Isurus* sp. were selected for the subsequent analyses, even if two of them lack part of the root.
396
397 *4.2. Shark tooth micro- and ultra-structure*
398 Most of the analyzed specimens, belonging to Lamniformes, exhibit a well preserved osteodont
399 histotype, whereas the carcharhiniform *Physogaleus contortus* displays an orthodont histotype (Fig.
400 1). No differences in microscopic preservation were noticed across the localities, and all the best
401 preserved teeth (including the Media Luna specimens with partial roots) exhibit a well preserved
402 histological microstructure (Fig. 5A).
403 Lamniform fossil teeth are comprised of a hypermineralized outer tissue layer, the enameloid,
404 and a core of dentine with a bone-like appearance, the osteodentine (Jambura et al., 2020) (Fig. 5).
405 All the analyzed teeth preserve their original histological features, such as a triple layered
406 enameloid in the outer part of the crown, and dentinal tubules forming osteons with clear lamellae
407 in the inner part of the crown and in the root. In addition, one tooth of *Cosmopolitodus hastalis*
408 from the eurhinodelphinid-like odontocete locality south of Cerro Colorado preserves a peculiar
409 osteodentine provided with well preserved vascular canals that is known also as vasodentine (Jollie,
410 1962). This osteodentine modification lacks dentinal tubules but displays radiating capillary
411 channels (Fig. 5B). Coating the crown, the enameloid is few hundred μm thick. From outer to inner,
412 the three well recognizable enameloid layers are the Shiny-Layered Enameloid (SLE), the Parallel-
413 Bundled Enameloid (PBE) and the Tangled-Bundled Enameloid (TBE) (Cuny et al., 2001) (Fig.

5C-F). This compact, orderly, and homogeneous enameloid wrapping is distinctly separated from the porous, disorderly, and heterogeneous inner core of osteodentine by the dentine-enameloid junction, a transitional zone that is clearly visible in BSE images (Fig. 5D). The inner core of the crown and root is characterized by an osteodentine tissue crossed by several dentinal tubules forming osteons (Fig. 5G). The osteodentine is usually affected by fractures and cavities (Fig. 5C, E). In some cases, the dentinal tubules are filled by sediment particles (Fig. 5H). Only the tooth of the carchariniform species *P. contortus* from south of Cerro Colorado exhibits crown portion constituted by orthodentine (Fig. 5F), which appears as more compact and less porous than the osteodentine, which in turn forms the root.

Observing the tooth ultrastructure in SE images, the enameloid appears as formed by highly-ordered bundles of fluorapatite crystallites (Daculsi et al., 1980; Chen et al., 2014; Enax et al., 2014; Lübke et al., 2015; Wilmers et al., 2021), which are often well preserved, whereas the dentine is characterized by crystalline artefacts likely diagenetic in origin (Lübke et al., 2015). In particular, the enameloid shows well preserved, elongated micrometric crystallites that are arranged parallel to each other to form bundles (Fig. 6A, B), typical of TBE (Cuny et al., 2001; Wilmers et al., 2021). On the other side, by analyzing the osteodentine portion, it is possible to encounter randomly oriented, disordered, sheet-shaped crystals, around one micron in size (Fig. 6C, D). These crystals probably represent the dentinal tubule infill of crystalline artefacts formed during diagenesis (Lübke et al., 2015).

In one case, in the Media Luna *M. paradoxodon* tooth, the osteodentine forming the root is pervasively affected by microborings that excavate the outermost portion of the root (Fig. 6E). These microborings have a diameter of 3–10 μm and a variable length, up to few tens of microns; furthermore, they display a distinctive brighter rim in BSE images (Fig. 6E, G). They are filled with apatite spherules and Fe-oxide framboids, which are visible in the SE and BSE images, as well as in Fe compositional map (Fig. 6E-H). Teeth with microborings must be discarded from the sampling

for SIS analyses, because their Sr ratio could be modified by secondary minerals filling the pores (Hoppe et al., 2003).

4.3. Shark tooth composition

Differences between enameloid and osteodentine are also clearly discernable by virtue of their chemical (major and trace element) composition.

EDS compositional maps across the dentine-enameloid junction reveal differences in the distribution of Ca, P, F, Na, Cl and S (Fig. 7, Table 2). In particular, the enameloid is generally enriched in F, Ca and P (Fig. 7C, D, Table 2), whereas the osteodentine is usually enriched in extraneous elements such as S, Na, and Cl (Fig. 7A-F, Table 2). In one case, we observed that the transition zone between the TBE and the osteodentine features a meshwork of fibers (Moyer et al., 2015) surrounding the osteodentine tissue and dentinal tubules that is similar in composition to the enameloid crystallites, whereas the composition of the dentinal tubules is close to that of the osteodentine, i.e. enriched in S (Fig. 7G, H).

Compositional maps also highlight the presence of a thin SLE, as reported by Enax et al. (2014). This external, shiny layer is enriched in Mg and Fe, and reveals an outermost depletion in F that is immediately followed inwards by a distinct increase in fluorine abundances (Fig. 8A-D). The compositional maps demonstrate that the shiny layer, though only few micron thick, is still well preserved, highlighting the good preservation of the analyzed fossil teeth.

Fe, Mn, Mg and Sr concentrations were measured through ICP-OES for checking alterations in both biogenic carbonates and phosphates (e.g., John et al., 2013; Ullmann and Korte, 2015). In the two oyster samples, the Fe content is low, being comprised between 68 and 215 ppm; the Mn content varies from 314 to 478 ppm; the Mg content is in the 2064–3260 ppm range; and the Sr content reflects that of unaltered oysters, ranging between 530 and 594 ppm (Table 3). In the shark teeth, the Fe content ranges from 713 to 2303 ppm; the Mn content spans from 54 and 225 ppm;

and the Mg content is within the 789–1717 ppm range (Table 3); and the Sr content, spanning between 1669–2332 ppm, is in the range of recent and fossil teeth reported in literature (Fig. 9).

4.4. Strontium Isotope Stratigraphy of the Chilcatay strata

$^{87}Sr/^{86}Sr$ ages obtained for all the analyzed teeth with the LOESS 6 curve calibrated on GTS2020 (McArthur et al., 2020) constrain the Chilcatay strata to the lower Miocene, between ca. 22 Ma and 18 Ma (Table 1). Shark teeth from the same stratigraphic horizons and localities display consistent $^{87}Sr/^{86}Sr$ ratios, which support the conclusion that the samples retained the original seawater Sr isotope ratio (McArthur et al., 1990, 1994). South of Cerro Colorado, the shark teeth collected at the eurhinodelphinid-like odontocete locality from undifferentiated Chilcatay strata show very similar $^{87}Sr/^{86}Sr$ values in spite of belonging to three different taxa. In particular, the *Cosmopolitodus hastalis* and *Isurus oxyrinchus* samples give a corrected $^{87}Sr/^{86}Sr$ value of 0.708526, whereas the *Physogaleus contortus* tooth gives a ratio of 0.708530, resulting in preferred ages of 18.90 and 18.85 Ma, respectively (Table 1). The $^{87}Sr/^{86}Sr$ value calculated from these samples, 0.708528, and the referred 2s.e. correspond to a preferred age of 18.85 Ma, with a very narrow range of uncertainty between 18.9 Ma and 18.8 Ma (Table 4). Therefore, the stratigraphic horizon that entombs the eurhinodelphinid-like specimen south of Cerro Colorado is Burdigalian and may be assigned to the Ct1 sequence in light of its absolute age (see below) (Fig. 10). The two teeth of *C. hastalis* associated with the holotype of *Macrosqualodelphis ukupachai* display very similar $^{87}Sr/^{86}Sr$ ratios, with corrected values of 0.708527 and 0.708532, corresponding respectively to preferred ages of 18.80 Ma and 18.85 Ma (Table 1). Similar results were obtained from one of the two oyster samples collected in the same stratigraphic layer, which displays a $^{87}Sr/^{86}Sr$ corrected value of 0.708523 and a preferred age of 18.90 Ma (Table 1). In turn, another oyster sample gives a higher $^{87}Sr/^{86}Sr$ ratio of 0.708573 and a preferred age of 18.25 Ma (Table 1), which is slightly younger than those obtained from the other samples from the same stratigraphic layer. Since both the oyster samples exhibit very well preserved prismatic layers without diagenetic imprints, there is

no valid reason to decide to choose one of the age values and discard the other. That said, the $^{87}Sr/^{86}Sr$ mean value calculated from the four samples (0.708539) and its 2s.e. result in an age range spanning from 19.1 Ma to 18.3 Ma, with a preferred age of 18.70 Ma (Table 4). This age estimate perfectly overlaps the previous radiometric dating of a volcanic ash layer (CHILC-AT1) sampled in the vicinities of the *M. ukupachai* specimen, which provided a $^{40}Ar/^{39}Ar$ age of 18.78 ± 0.08 Ma (Bianucci et al., 2018a); hence, it confirms a Burdigalian age for this cetacean species as well as for the Chilcatay deposits exposed in the surrounding area.

At Zamaca, at the base of the Ct2 sequence (ShB-4 tooth bed), two shark teeth display concordant $^{87}Sr/^{86}Sr$ corrected ratios of 0.708569 and 0.708576, thus resulting into preferred ages of 18.30 Ma and 18.20 Ma (Table 1). The preferred age obtained from the calculated $^{87}Sr/^{86}Sr$ mean value (0.708573) for the stratigraphic layer is 18.25 Ma, with a maximum age of 18.4 Ma and a minimum age of 18.1 Ma (Table 4). These results confirm the Burdigalian age of the Ct2 sequence and are perfectly concordant with a $^{40}Ar/^{39}Ar$ age of 18.02 ± 0.07 Ma obtained from a volcanic ash layer (SOT-T3) from the very top of the Ct2 sequence in the neighboring locality of Ullujaya (Di Celma et al., 2018b).

Twenty-five km west of the Ica River, at Media Luna, four teeth of *Isurus* sp. from the same stratigraphic horizon give slightly different corrected $^{87}Sr/^{86}Sr$ values, ranging from 0.708415 to 0.708364, resulting in preferred ages of 21.95 Ma, 21.20 Ma, 20.45 Ma and 20.20 Ma, respectively (Table 1). Although the preservation of the *Isurus* teeth is not optimal, there are no reasons to prefer one tooth to another, and all these samples were included in the final age calculation. A $^{87}Sr/^{86}Sr$ mean value of 0.708383 was calculated, resulting in a time span of 21.8–20.1 Ma, with a preferred age of 20.90 Ma (Table 4), corresponding to an Aquitanian to very early Burdigalian age for the Chilcatay strata exposed at Media Luna.

5. Discussion

5.1. Evaluating the shark tooth diagenesis

Fossil shark teeth can survive geological time because of their resistance to alteration. In addition, shark cyclically replace their teeth during lifetime. As a likely consequence of both taphonomic conditions favoring preservation and an original abundance of shark life, the fossil record of the Pisco Basin is characterized by rich tooth-bearing intervals (Renz, 2009; Ehret et al., 2012; Bianucci et al., 2018b; Di Celma et al., 2019; Landini et al., 2019; Collareta et al., 2021b). In particular, fossil shark teeth from the Chilcatay Formation can be found accumulated in specific layers (e.g., the Zamaca tooth-bearing ShB-4 horizon, at the base of Ct2 Chilcatay sequence; and the shark tooth-bearing Terrace 1 horizon at Media Luna, in Chilcatay undifferentiated strata) and associated to other marine vertebrates (e.g., south of Cerro Colorado, at the eurhinodelphinid-like odontocete and *Macrosqualodelphis ukupachai* localities, in Chilcatay undifferentiated strata).

All the analyzed fossil teeth from these localities and stratigraphic intervals are from moderately to well preserved, showing no macroscopical evidence of wear, bioerosion or encrustation. Only the teeth collected at Media Luna lack root portions or show, in one case, microborings affecting the outermost portion of the root. Specifically, the boring outline and dimensions are consistent with the Type B microborings of Gariboldi et al. (2015) and the linear longitudinal tunnels of Jans (2008). The rim that appears brighter in BSE images and the stippled apatite infill suggest an origin from bacterial activity (Jans, 2008), as well as the presence of Fe-oxide framboidal ghosts of pyrite (Pfretzschner, 2001a, b; Gariboldi et al., 2015; Bosio et al., 2021b). Since strong evidence of erosion, transport and encrustation is absent, the lack of root portions could be due to erosion in a recent desert and coastal environment; on the other hand, the presence of microborings of bacterial origin could be indicative of a short period of starvation at the seafloor, suggesting a condensed lag origin for the Terrace 1 tooth-bearing horizon at Media Luna, thus also explaining the slight differences observed in the obtained Sr ages (see below). That said, all the analyzed teeth, including the Media Luna samples, exhibit micro- and ultra-structural histological features that recall those of modern and unaltered teeth and hint at the lack of diagenetic alteration. In detail, both the osteodont (Lamniformes) and orthodont (Carcharhiniformes) teeth display a well preserved hypermineralized

outer layer comprised of enameloid. Under the optical and electronic microscopes, the three constituting layers of the enameloid wrapping (SLE, PBE and TBE) are easily recognizable. The enameloid is compact and formed by highly ordered, elongated bundles of fluorapatite crystallites (Daculsi et al., 1980; Chen et al., 2014; Enax et al., 2014; Lübke et al., 2015; Wilmers et al., 2021). On the other hand, the osteodont histotype exhibits a tooth core of osteodentine, a tissue that is very similar to the compact bone (Jambura et al., 2020), having a porous, disorderly and heterogeneous appearance, and sometimes fractures. The dentinal tubules permeating the osteodentine are in some cases filled by sediment particles or by randomly oriented, disordered, sheet-shaped, micrometric crystals, which are here interpreted as crystalline artefacts that formed during diagenesis (Lübke et al., 2015). The analyzed orthodont histotype exhibits a core of a more compact tissue permeated by small parallel tubules surrounding a large inner cavity, i.e. the pulp cavity (Moyer et al., 2015). The root of the orthodont histoytpe is however comprised of osteodentine, with large dentinal tubules that form osteons. Our results contribute to further highlight the intrinsic differences between the enameloid and dentine tissues. The high porosity and low resistance make the latter a bad source material for isotope analyses (Becker et al., 2008; Enax et al., 2012, 2014; Tütken et al., 2020).

The teeth selected for SIS display major and trace elemental abundances that are consistent with those of teeth from recent lamniform sharks. Ca, P, F, Na, Cl and S concentrations match well the data by Enax et al. (2012, 2014), Lübke et al. (2015), and Kocsis et al. (2015) for recent and fossil shark species. In addition, the high degree of preservation of the SLE is demonstrated also by its distinctive chemical composition as exemplified by differences in Mg, Fe and F content compared to the underlying PBE and TBE layers. The higher Na, Cl and S contents of osteodentine could be related to the presence of secondary minerals such as halite and gypsum/anhydrite in the cavities of the tooth tissue: in fact, the high porosity of the osteodentine could allow for fluid penetration and precipitation of secondary minerals during late diagenesis, as has been reported elsewhere for fossil bones from the Chilcatay and Pisco formations (Gioncada et al., 2018a, b; Bosio et al., 2021c). Moreover, looking at the values of the EDS totals, the sum for the enameloid layer is regularly close

568 to 100%, whereas the sum for the dentine is <100 wt% (Table 2). This is probably due to the
569 presence of carbonate and hydroxyl groups which are not measured by EDS (Møller et al., 1975;
570 Bosio et al., 2021c) as well as to the low compactness of dentine to enameloid.

571 Fe, Mn, Mg, and Sr concentrations measured by means of ICP-OES can be informative in terms
572 of diagenetic imprint on carbonates (e.g., Ullmann and Korte, 2015): usually, the Fe and Mn
573 contents increase during diagenesis, whereas the Mg and Sr abundances generally decrease during
574 diagenesis. For the two oysters analyzed in this study, the trace element concentrations are in line
575 with those of unaltered fossil oysters in the Chilcatay Formation (Bosio et al., 2020a) and within the
576 limits reported by Ullmann and Korte (2015) for regarding them as not affected by a strong
577 diagenetic imprint. Mn and Sr contents have been reported to be useful for establishing the
578 diagenetic impact for biogenic phosphates like those that comprise bones and teeth (Nelson et al.,
579 1986; Elorza et al., 1999; Kohn et al., 1999; Martin and Scher, 2004; Piga et al., 2011;
580 Dericquebourg et al., 2019; Golding and McMillan, 2020; Bosio et al., 2021c); that said, in modern
581 shark teeth, these element concentrations could also be very variable, both within and across
582 different species (Vennemann et al., 2001; Nemliher et al., 2004; Becker et al., 2008; John et al.,
583 2013; Kocsis et al., 2015; Malferrari et al., 2019). As regards our samples, trace element
584 compositions are quite in line with those of both modern and fossil shark teeth, hence confirming a
585 low diagenetic imprint. In detail, the Fe content is higher than those reported for recent
586 carcharhinids (John et al., 2013; Kocsis et al., 2015), but lower than that of *Galeocerdo cuvier* (John
587 et al., 2013). On the other hand, Fe values are in agreement with those of the Paleogene lamniform
588 *Otodus* sp. and living lamniform species (John et al., 2013; Malferrari et al., 2019). In general, the
589 Mn content is higher than those of all the recent carcharhiniforms and lamniforms reported by John
590 et al. (2013) and Kocsis et al. (2015), with small differences relative to *Carcharhinus limbatus* and
591 *Carcharhinus obscurus*. Such differences could be related to the ubiquitous presence of Mn oxides
592 in the Ica Desert (Gioncada et al., 2018a, b). The Mg content is also in good agreement with those
593 reported for modern carcharhinids (John et al., 2013; Kocsis et al., 2015), as well as for Paleogene

Otodus specimens and living lamniform species (Malferrari et al., 2019), but are respectively higher and lower than those of *C. limbatus* and *Prionace glauca* (John et al., 2013). Finally, the Sr content is still in the range of both recent (Vennemann et al., 2001; Becker et al., 2008; John et al., 2013; Kocsis et al., 2015) and fossil (Grandjean et al., 1987; Schmitz et al., 1991; Vennemann and Hegner, 1998; Martin and Scher, 2004; Becker et al., 2008) lamniform and carcharhiniform shark teeth, with the majority of the values falling in the 1000–3000 ppm range (Figure 9), and far from the Sr concentrations (ca. 5000 ppm) of the diagenetically altered fish teeth studied by Martin and Scher (2004). All things considered, the shark teeth that were selected for SIS might be regarded as retaining the pristine Sr isotope ratio of the paleo-seawater.

5.2. Chilcatay chronostratigraphy

When compared to the LOESS 6 calibrated on GTS2020 (McArthur et al., 2020), our $^{87}Sr/^{86}Sr$ results give Burdigalian ages between 19.1 Ma and 18.1 Ma for the Chilcatay strata at the Ica River Valley localities of Zamaca and south of Cerro Colorado (Table 4), thus confirming previous radiometric, isotopic and biostratigraphic ages (Di Celma et al., 2018b; Lambert et al., 2018; Bosio et al., 2020a, b). For a deeper comparison between the previous SIS results provided by Bosio et al. (2020a) and those obtained in the present work, the former have been recalculated herein using the LOESS 6 calibrated on GTS2020 (McArthur et al., 2020) (Table 5). Thus, the basal Pisco (P0) strata exposed at Cerro Submarino and nearby localities (Bosio et al., 2020a; Collareta et al., 2021a) are here referred to the 14.7–12.6 Ma time span, whereas the *Ct1c* facies association found at the base of the Ct1 sequence at Roca Negra is dated at 18.80 Ma, with a range between 19.1 Ma and 18.7 Ma (Table 5, Fig. 10). The overlying *Ct1a* facies association at Ullujaya is dated between 18.9 Ma and 18.3 Ma, with the three layers giving preferred ages of 18.82 Ma, 18.58 Ma and 18.57 Ma, respectively (Table 5, Fig. 10).

Therefore, the undifferentiated strata of the Chilcatay Formation exposed at the two localities south of Cerro Colorado (i.e. at the eurhinodelphinid-like and *Macrosqualodelphis ukupachai* finding

sites) should be attributed to the base of the Ct1 sequence, dated to ca. 19–18 Ma by means of both radiometric and biostratigraphic methods at the Ullujaya and Roca Negra localities (Di Celma et al., 2018b; Lambert et al., 2018; Bosio et al., 2020a, b). Indeed, the teeth associated with the eurhinodelphinid-like specimen give a preferred age of 18.85 Ma, with a very small range between 18.9 Ma and 18.8 Ma, whereas teeth and oysters collected in association with *M. ukupachai* reveal a preferred age of 18.7 Ma, with an error spanning from 19.1 Ma to 18.3 Ma (Fig. 10). These results are in excellent agreement with the age of 18.78 ± 0.08 Ma attributed by means of $^{40}Ar/^{39}Ar$ dating to a volcanic ash layer sampled at 1.7 km SE of the *M. ukupachai* holotype and near an uncollected squalodelphinid skeleton most likely belonging to the same taxon (Bianucci et al. 2018a). At Zamaca, the base of the Ct2 sequence is dated herein for the first time. Our results attribute a preferred age of 18.25 Ma to the tooth-bearing ShB-4 horizon, with a range extending from 18.4 Ma to 18.1 Ma (Fig. 10), in excellent agreement with the underlying Ct1 ages as well as with the radiometric age of 18.02 ± 0.07 Ma from a volcanic ash layer sampled near the top of Ct2 at Ullujaya (Di Celma et al., 2018b). On the whole, these new age estimates allow for increasing the age resolution for the marine vertebrate-bearing localities of Ullujaya and Zamaca, thus highlighting differences in the taxonomic composition of the odontocete assemblages at different localities where roughly coeval strata are exposed. Indeed, *M. ukupachai* and the eurhinodelphinid-like odontocete found south of Cerro Colorado are dated at ca. 18.85–18.7 Ma, whereas *Huaridelphis*, *Chilcacetus*, *Notocetus*, *Raphicetus*, cf. *Eurhinodelphis* sp., *Ensidelphis riveroi* and *Inticetus vertizi* from Ullujaya and Zamaca belong to the ca. 18.8–18.6 Ma time span (Bianucci et al., 2015, 2018a, b, 2020; Lambert et al., 2014, 2015, 2017, 2020, 2021; Bianucci and Collareta, 2022). Since the aforementioned age intervals appear as substantially indistinguishable, a paleogeographical and/or paleoecological explanation may be hypothesized for explaining the observed taxonomic differences.

Finally, the Chilcatay strata cropping out at Media Luna are dated herein for the first time, obtaining a preferred age of 20.9 Ma for the tooth-bearing Terrace 1 horizon, with a rather wide

time range between 21.8 and 20.1 Ma (late Aquitanian-early Burdigalian) (Fig. 10). Differences in the individual age estimates obtained for the four teeth analyzed from this horizon could be related to the intrinsic sedimentological origin of this shark tooth accumulation, whose preservation state suggests a prolonged exposition at the seafloor (with the teeth having the time to loose their roots and being affected by bacterial bioerosion). However, these data are nonetheless important as they allow for attributing the as yet undifferentiated Chilcatay strata exposed at Media Luna to an older sequence compared to Ct1 and Ct2; this stratal package may coincide with the Chilcatay-0 (Ct0) strata reported from the Laberinto locality by DeVries et al. (2021). The ongoing investigation of the lower Chilcatay strata of Media Luna can thus be anticipated to disclose important and novel information on the basal Miocene marine vertebrate assemblages of the Pisco Basin.

All things considered, the overall consistency of the strontium ages obtained at different localities where the Chilcatay Formation is exposed confirms the suitability of the SIS methods for dating both carbonates and phosphates in this basin. Furthermore, and perhaps more importantly, these results strengthen the notion that the Sr-ratio of shark teeth can be successfully used for getting reliable age estimates by means of SIS. Even if macroscopical observations could be far from promising, shark teeth have the capability of retaining their microscopical histology and composition through geological time, thus allowing for reliable isotope results if only the enameloid is sampled.

6. Conclusions

Teeth are the most common fossil remains of marine vertebrates, and provide a precious source material for chronostratigraphic and paleoecological purposes. Shark teeth of Lamniformes and Carchariniformes from the Miocene deposits of the Peruvian Pisco Basin were analyzed for better defining the chronostratigraphy of the Chilcatay Formation through the application of the Strontium Isotope Stratigraphy (SIS). Fossil teeth exhibit a compact and well preserved enameloid layer that is well distinct from the porous and heterogeneous dentine. Ultrastructural analyses show

highly ordered and well preserved bundles of fluorapatite crystallites forming the enameloid layer, whereas dentine exhibits a bone-like structure (i.e. the osteodentine) showing tubules and crystalline artefacts due to diagenesis. In a single case, the trabecular dentine constituting the tooth root is affected by microborings filled with apatite spherules and Fe-oxide framboids. Compositional analyses highlight differences concerning the distribution of Ca, P, F, and S in the enameloid and dentine, and reveal the presence of the Shiny-Layered Enameloid (SLE), thus indicating a good preservation state. In addition, the Sr contents of the analyzed teeth are comparable with those of teeth from recent sharks. Based on these results, eleven shark teeth were selected for $^{87}Sr/^{86}Sr$ analyses. By comparing our Sr results with the LOESS database calibrated to GTS2020, a Burdigalian age (19.1–18.1 Ma) is obtained for the Chilcatay Formation cropping out at Zamaca and south of Cerro Colorado in the Ica River Valley, which matches well previous radioisotopic and biostratigraphic ages. At Media Luna, 25 km west of the Ica River, shark teeth give ages of 21.8–20.1 Ma, revealing a new sequence deposited between the late Aquitanian and the earliest Burdigalian. Thus, our new results allow for better defining the chronostratigraphy of the Chilcatay Formation in the Pisco Basin. Furthermore, they strengthen the notion that $^{87}Sr/^{86}Sr$ dating can be successfully retrieved from fossil shark teeth to obtain reliable age estimates.

Acknowledgments

The authors wish to thank S. Riechelmann for running the ICP-OES and Sr isotope analyses at Bochum University, TS Lab & Geoservices snc for realizing thin sections, T. Catelani for the help with SEM-EDS analyses, and J. McArthur for sharing the LOESS 6 Table. A special thank to A. Gioncada, E. Malinverno, P.P. Pierantoni, K. Gariboldi, G. Molli, G. Sarti, O. Lambert, F.G. Marx, C. de Muizon, T.J. DeVries, for fruitful discussions about the paleontology and geology of the Pisco Basin. The authors also thank W. Aguirre, J. Chauca-Luyo, P. Giuffra for their assistance in the field, and R. Varas-Malca and R. Salas-Gismondi for their support at the Museo de Historia Natural de la Universidad Nacional Mayor de San Marcos (Lima).

Funding

This study was supported by grants from the Italian Ministero dell'Istruzione dell'Università e della Ricerca to G.Bi. (PRIN Project 2012YJSBMK), from the Università of Pisa (PRA_2017_0032 to G.Bi.), and from the Università di Camerino (FAR 2019, STI000102 to C.D.C.). This study was also funded by a grant from the Università degli Studi di Milano-Bicocca ("Premio Giovani Talenti" 2020-ATESP-0121 to G.B.) and by National Geographic Society Committee for Research Exploration grant (9410-13 to G.Bi.).

References

Acosta-Hospitalache, C., Strucchi, M., 2005. Nuevos restos terciarios de Spheniscidae (Aves, Sphenisciformes) procedentes de la costa del Perú. Spanish Journal of Palaeontology, 20 (1), 1-5.

Akhtar, A.A., Santi, L.M., Griffiths, M.L., Becker, M., Eagle, R.A., Kim, S., Kocsis, L., Rosenthal, Y., Higgins, J.A., 2020. A record of the δ44/40Ca and [Sr] of seawater over the last 100 million years from fossil elasmobranch tooth enamel. Earth and Planetary Science Letters, 543, 116354.

Alleman, V., 1978. Estudio de los macrofósiles del Mioceno de la costa peruana. Revista Universidad Particular "Ricardo Palma", 1, 88-115.

Alván De la Cruz, A., 2008. Geología de Ocucaje: aportes en la sedimentología y paleontología de Lomas de Ullujaya (Ica, Perú). Revista del Instituto de Investigaciones FIGMMG, 11 (21), 51-59.

Ayliffe, L.K., Chivas, A.R., Leakey, M.G., 1994. The retention of primary oxygen isotope compositions of fossil elephant skeletal phosphate. Geochimica et Cosmochimica Acta, 58(23), 5291-5298.

Barrat, J.A., Taylor, R.N., Andre, J.P., Nesbitt, R.W., Lecuyer, C., 2000. Strontium isotopes in biogenic phosphates from a neogene marine formation: implications for palaeoseawater studies. Chemical Geology, 168 (3-4): 325-332.

724 Becker, M.A., Seidemann, D.E., Chamberlain, Jr J.A., Buhl, D., Slattery, W., 2008. Strontium
725 isotopic signatures in the enameloid and dentine of upper Cretaceous shark teeth from western
726 Alabama: paleoecologic and geochronologic implications. Palaeogeography, Palaeoclimatology,
727 Palaeoecology, 264 (1-2): 188-194.
728 Bianucci, G., Bosio, G., Malinverno, E., Muizon, C. de, Villa, I.M., Urbina, M., Lambert, O.,
729 2018a. A new large squalodelphinid (Cetacea, Odontoceti) from Peru sheds light on the Early
730 Miocene platanistoid disparity and ecology. Royal Society Open Science, 5(4), 172302.
731 Bianucci, G., Collareta, A., Bosio G., Landini, W., Gariboldi, K., Gioncada, A., Lambert, O.,
732 Malinverno, E., Muizon, C. de, Varas-Malca, R., Villa, I.M., Coletti, G., Urbina, M., Di Celma,
733 C., 2018b. Taphonomy and palaeoecology of the lower Miocene marine vertebrate assemblage
734 of Ullujaya (Chilcatay Formation, East Pisco Basin, southern Peru). Palaeogeography
735 Palaeoclimatology Palaeoecology, 511, 256-279.
736 Bianucci, G., Collareta, A., 2022. An overview of the fossil record of cetaceans from the Pisco
737 Basin (Peru). Bollettino della Società Paleontologica Italiana, 61(1), 19-60.
738 Bianucci, G., Muizon, C. de, Urbina, M., Lambert O., 2020. Extensive diversity and disparity of the
739 early miocene Platanistoids (Cetacea, Odontoceti) in the Southeastern Pacific (Chilcatay
740 Formation, Peru). Life, 10(3), 27.
741 Bianucci, G., Urbina, M., Lambert, O., 2015. A new record of *Notocetus vanbenedeni*
742 (Squalodelphinidae, Odontoceti, Cetacea) from the Early Miocene of Peru. Comptes Rendus
743 Palevol, 14(1), 5-13.
744 Boskovic, D.S., Vidal, U.L., Nick, K.E., Esperante, R., Brand, L.R., Wright, K.R., Sandberg, L.B.,
745 Siviero, B.C.T., 2021. Structural and protein preservation in fossil whale bones from the Pisco
746 Formation (Middle-Upper Miocene), Peru. Palaios., 36, 155–164.
747 Bosio, G., Malinverno, E., Collareta, A., Di Celma, C., Gioncada, A., Parente, M., Berra, F., Marx,
748 F.G., Vertino, A., Urbina, M., Bianucci, G., 2020a. Strontium isotope stratigraphy and the

thermophilic fossil fauna from the middle Miocene of the East Pisco Basin (Peru). J. S. Am. Earth Sci. 97, 102399. https://doi.org/10.1016/j.jsames.2019.102399

Bosio, G., Malinverno, E., Villa, I.M., Di Celma, C., Gariboldi, K., Gioncada, A., Barberini, V., Urbina, M., Bianucci G., 2020b. Tephrochronology and chronostratigraphy of the Miocene Chilcatay and Pisco formations (East Pisco basin, Peru). Newsletters on Stratigraphy, 53 (2), 213-247.

Bosio, G., Bracchi, V., Malinverno, E., Collareta, A., Coletti, G., Gioncada, A., Kočí, T., Di Celma, C., Bianucci, G., Basso, D., 2021a. Taphonomy of a *Panopea* Ménard de la Groye, 1807 shell bed from the Pisco Formation (Miocene, Peru). Comptes Rendus Palevol, 20(8), 119-140.

Bosio, G., Collareta, A., Di Celma, C., Lambert, O., Marx, F. G., de Muizon, C., Gioncada, A., Gariboldi, K., Malinverno, E., Varas Malca, R., Urbina, M, Bianucci, G., 2021b. Taphonomy of marine vertebrates of the Pisco Formation (Miocene, Peru): Insights into the origin of an outstanding Fossil-Lagerstätte. PLoS One, 16(7), e0254395.

Bosio, G., Gioncada, A., Gariboldi, K., Bonaccorsi, E., Collareta, A., Pasero, M., Di Celma, C., Malinverno, E., Bianucci, G., 2021c. Mineralogical and geochemical characterization of fossil bones from a Miocene marine Konservat-Lagerstätte. Journal of South American Earth Sciences, 105, 102924.

Botella, H., Donoghue, P.C.J., Martínez-Pérez, C., 2009. Enameloid microstructure in the oldest known chondrichthyan teeth. Acta Zoologica, 90, 103-108.

Brand, L.R., Esperante, R., Chadwick, A.V., Poma Porras, O., Alomía, M., 2004. Fossil whale preservation implies high diatom accumulation rate in the Miocene-Pliocene Pisco Formation of Peru. Geology, 32, 165-168.

Brand, L.R., Urbina, M., Chawick, A., DeVries, T.J., Esperante, R., 2011. A high resolution stratigraphic framework for the remarkable fossil cetacean assemblage of the Miocene/Pliocene Pisco Formation, Peru. Journal of South American Earth Sciences, 31, 414–425. doi:10.1016/j.jsames.2011.02.015

775 Brunet, F., Allan, D. R., Redfern, S. A., Angel, R. J., Miletich, R., Reichmann, H. J., Sergent, J.,
776 Hanfland, M., 1999. Compressibility and thermal expansivity of synthetic apatites, Ca5(PO4)3X
777 with X= OH, F and Cl. European Journal of Mineralogy, 11(6), 1023-1035.
778 Burke, W.H., Denison, R.E., Hetherington, E.A., Koepnick, R.B., Nelson, H.F., Otto, J.B., 1982.
779 Variation of seawater 87Sr/86Sr throughout Phanerozoic time. Geology, 10(10), 516-519.
780 Cappetta, H., 2012. Chondrichthyes. Mesozoic and Cenozoic Elasmobranchii Teeth. Pfeil-Verlag,
781 Munich, 512 p.
782 Carlson, S.J., 1990. Vertebrate dental structures. Skeletal biomineralization: patterns, processes and
783 evolutionary trends, 5, 235-260.
784 Chen, C., Wang, Z., Saito, M., Tohei, T., Takano, Y., Ikuhara, Y., 2014. Fluorine in shark teeth: Its
785 direct Atomic-Resolution imaging and strengthening function. Angewandte Chemie, 126(6),
786 1569-1573.
787 Cleveland, W.S., 1981. LOWESS - a program for smoothing scatterplots by robust locally weighted
788 regression. American Statistician, 35 (1), 54.
789 Colbert, E.H., 1944. A new fossil whale from the Miocene of Peru. Bulletin of the American
790 Musem of Natural History, 83, 195-216.
791 Coletti, G., Bosio, G., Collareta, A., Buckeridge, J., Consani, S., El Kateb, A., 2018.
792 Palaeoenvironmental analysis of the Miocene barnacle facies: case studies from Europe and
793 South America. Geol. Carpathica 69, 573–592.
794 Coletti, G., Bosio, G., Collareta, A., Malinverno, E., Bracchi, V., Di Celma, C., Basso, D.,
795 Stainbank, S., Spezzaferri, S., Cannings, T., Bianucci, G., 2019a. Biostratigraphic, evolutionary,
796 and paleoenvironmental significance of the southernmost lepidocyclinids of the Pacific coast of
797 South America (East Pisco Basin, southern Peru). J. S. Am. Earth Sci., 96, 102372.
798 https://doi.org/10.1016/j.jsames.2019.102372.

799 Coletti, G., Collareta, A., Bosio, G., Buckeridge, J., Urbina M., 2019b. *Perumegabalanus calziai*
800 gen. et sp. nov., a new intertidal megabalanine barnacle from the early Miocene of Peru. Neues
801 Jahrbuch fur Geologie und Palaontologie-Abhandlungen, 294(2), 197-212.
802 Collareta, A., Coletti, G., Bosio, G., Buckeridge, J., de Muizon, C., DeVries, T.J., Varas-Malca, R.,
803 Altamirano-Sierra, A., Urbina-Schmitt, M., Bianucci, G., 2019. A new barnacle (Cirripedia:
804 Neobalanoformes) from the early Miocene of Peru: palaeoecological and palaeobiogeographical
805 implications. Neues Jahrb. Geol. Palaontol. Abh. 292, 321-338.
806 Collareta, A., Di Celma, C., Bosio, G., Pierantoni, P.P., Malinverno, E., Lambert, O., Marx, F.G.,
807 Landini, W., Urbina, M., Bianucci, G., 2021a. Distribution and paleoenvironmental framework
808 of middle Miocene marine vertebrates along the western side of the lower Ica Valley (East Pisco
809 Basin, Peru). Journal of Maps, 17(2), 7-17.
810 Collareta A., Lambert O., Marx F.G., Muizon C. de, Varas-Malca R., Landini W., Bosio G.,
811 Malinverno E., Gariboldi K., Gioncada A., Urbina M., Bianucci, G., 2021b. Vertebrate
812 Palaeoecology of the Pisco Formation (Miocene, Peru): Glimpses into the Ancient Humboldt
813 Current Ecosystem. Journal of Marine Science and Engineering, 9 (11): 1188.
814 Compagno, L.J.V., 1988. Sharks of the Order Carcharhiniformes. Princeton, NJ: Princeton
815 University Press.
816 Cuny, G., Risnes, S., 2005. The enameloid microstructure of the teeth of synechodontiform sharks
817 (Chondrichthyes: Neoselachii). PalArch's Journal of Vertebrate Palaeontology, 3(2), 1-19.
818 Cuny, G., Rieppel, O., Sander, P.M., 2001. The shark fauna from the Middle Triassic (Anisian) of
819 north-western Nevada. Zoological Journal of the Linnean Society, 133(3), 285-301.
820 Daculsi, G., Kerebel, L.M., 1980. Ultrastructural study and comparative analysis of fluoride content
821 of enameloid in sea-water and fresh-water sharks. Archives of Oral Biology, 25(3), 145-151.
822 Dahm, S., Risnes, S., 1999. A comparative infrared spectroscopic study of hydroxide and carbonate
823 absorption bands in spectra of shark enameloid, shark dentin, and a geological apatite. Calcified
824 Tissue International, 65(6), 459-465.

825 DePaolo, D.J., Ingram, B.L., 1985. High-resolution stratigraphy with strontium isotopes. Science,
826 227(4689), 938-941.
827 Dericquebourg, P., Person, A., Ségalen, L., Pickford, M., Senut, B., Fagel, N., 2019. Bone
828 diagenesis and origin of calcium phosphate nodules from a hominid site in the Lukeino
829 Formation (Tugen Hills, Kenya). Palaeogeography, Palaeoclimatology, Palaeoecology, 536,
830 109377.
831 DeVries, T.J., 1988. Mollusks of the Pisco Basin. Pisco Basin Guidebook, 8, 127-134.
832 DeVries, T.J., 1998. Oligocene deposition and Cenozoic sequence boundaries in the Pisco Basin
833 (Peru). J. South Am. Earth Sci. 11, 217–231.
834 DeVries, T.J., 2017. Eocene Stratigraphy and Depositional History near Puerto Caballas (East Pisco
835 Basin, Peru). Boletín de la Sociedad Geológica del Perú 112, 39–52.
836 DeVries, T.J., Frassinetti, D., 2003. Range extensions and biogeographic implications of Chilean
837 Neogene mollusks found in Peru. Boletín del Museo Nacional de Historia Natural, Chile 52,
838 119–135.
839 DeVries, T.J., Jud, N.A., 2018. Lithofacies patterns and paleogeography of the Miocene Chilcatay
840 and lower Pisco depositional sequences (East Pisco Basin, Peru). Bol. Soc. Geol. Perú, 8, 124-
841 167.
842 DeVries, T.J., Barron, J.A., Urbina-Schmitt, M., Ochoa, D., Esperante, R., Snee, L.W., 2021. The
843 Miocene stratigraphy of the Laberinto area (Río Ica Valley) and its bearing on the geological
844 history of the East Pisco Basin (south-central Peru). Journal of South American Earth Sciences,
845 111, 103458.
846 DeVries, T.J., Urbina, M., Jud, N.A., 2017. The Eocene-Oligocene Otuma Depositional Sequence
847 (East Pisco Basin, Peru): Paleogeographic and Paleoceanographic Implications of New Data.
848 Boletín de la Sociedad Geológica del Perú 112, 14–38.
849 Di Celma, C., Malinverno, E., Bosio, G., Collareta, A., Gariboldi, K., Gioncada, A., Molli, G.,
850 Basso, D., Varas-Malca, R.M., Pierantoni, P.P., Villa, I.M., Lambert, O., Landini, W., Sarti, G.,

Cantalamessa, G., Urbina, M., Bianucci, G., 2017. Sequence stratigraphy and paleontology of the upper Miocene Pisco Formation along the western side of the lower Ica valley (Ica Desert, Peru). Riv. Ital. Paleontol. Stratigr. 123, 255–274. https://doi.org/10.13130/2039-4942/8373.

Di Celma, C., Malinverno, E., Bosio, G., Gariboldi, K., Collareta, A., Gioncada, A., Landini, W., Pierantoni, P.P., Bianucci, G. 2018a. Intraformational unconformities as a record of late Miocene eustatic falls of sea level in the Pisco Formation (southern Peru). Journal of Maps, 14, 607–619.

Di Celma, C., Malinverno, E., Collareta, A., Bosio, G., Gariboldi, K., Lambert, O., Landini, W., Gioncada, A., Villa, I.M., Coletti, G., Muizon, C. de, Urbina, M., Bianucci G., 2018b. Facies analysis, stratigraphy and marine vertebrate assemblage of the early Miocene Chilcatay Formation at Ullujaya (Pisco basin, Peru). Journal of Maps, 14(2), 257-268.

Di Celma, C., Pierantoni, P.P., Malinverno, E., Collareta, A., Lambert, O., Landini, W., Bosio G., Gariboldi, K., Gioncada, A., Muizon, de C., Molli, G., Marx, F.G., Varas-Malca, R.M., Urbina, M., Bianucci G., 2019. Allostratigraphy and paleontology of the lower Miocene Chilcatay Formation in the Zamaca area, East Pisco basin, southern Peru. Journal of Maps, 15(2), 393-405.

Di Celma, C., Pierantoni, P.P, Volatili, T., Molli, G., Mazzoli, S., Sarti, G., Ciattoni, S., Bosio, G., Malinverno, E., Collareta, A., Gariboldi, K., Gioncada A., Jablonska, D., Landini, W., Urbina, M., Bianucci, G., in press. Towards deciphering the Cenozoic evolution of the East Pisco Basin (southern Peru). Journal of Maps. https://doi.org/10.1080/17445647.2022.2072780

Dunbar, R.B., Marty, R.C., Baker, P.A., 1990. Cenozoic marine sedimentation in the Sechura and Pisco basins, Peru. Palaeogeogr. Palaeoclim. 77, 235–261.

Ehret, D.J., Macfadden, B.J., Jones, D.S., Devries, T.J., Foster, D.A., Salas-Gismondi, R., 2012. Origin of the white shark *Carcharodon* (Lamniformes: Lamnidae) based on recalibration of the Upper Neogene Pisco Formation of Peru. Palaeontology, 55(6), 1139-1153.

Elorza, J., Astibia, H., Murelaga, X., Pereda-Suberbiola, X., 1999. Francolite as a diagenetic mineral in dinosaur and other Upper Cretaceous reptile bones (Laño, Iberian Peninsula): microstructural, petrological and geochemical features. Cretaceous research, 20(2), 169-187.

877 Enax J., Janus A.M., Raabe D., Epple M., Fabritius H.O., 2014. Ultrastructural organization and
878 micromechanical properties of shark tooth enameloid. Acta biomaterialia, 10 (9): 3959-3968.
879 Enax J., Prymak O., Raabe D., Epple M., 2012. Structure, composition, and mechanical properties
880 of shark teeth. Journal of structural biology, 178 (3), 290-299.
881 Enault, S., Guinot, G., Koot, M. B., Cuny, G., 2015. Chondrichthyan tooth enameloid: past, present,
882 and future. Zoological Journal of the Linnean Society, 174(3), 549-570.
883 Esperante, R., Brand, L., Nick, K.E., Poma, O., Urbina, M., 2008. Exceptional occurrence of fossil
884 baleen in shallow marine sediments of the Neogene Pisco Formation, Southern Peru.
885 Palaeogeogr Palaeoclim., 257, 344–360.
886 Esperante, R., Brand, L.R., Chadwick, A.V., Poma, O., 2015. Taphonomy and paleoenvironmental
887 conditions of deposition of fossil whales in the diatomaceous sediments of the Miocene/Pliocene
888 Pisco Formation, southern Peru—a new Fossil-Lagerstätte. Palaeogeogr Palaeoclim., 417, 337–
889 370.
890 Faure, G., Mensing, T.M., 2005. Isotopes. Principles and applications. John Wiley & Sons, Inc., p.
891 897.
892 Francillon-Vieillot, H., de Buffrénil, V., Castanet, J., Géraudie, J., Meunier, F.J., Sire, J.Y.,
893 Zylbelberg, L., de Ricqlès, A., 1990. Microstructure and mineralization of vertebrate skeletal
894 tissues. Skeletal biomineralization: patterns, processes and evolutionary trends, 1, 471-530.
895 Frijia, G., Parente, M., Di Lucia, M., Mutti, M., 2015. Carbon and strontium isotope stratigraphy of
896 the Upper Cretaceous (Cenomanian-Campanian) shallow-water carbonates of southern Italy:
897 Chronostratigraphic calibration of larger foraminifera biostratigraphy. Cretaceous Research, 53,
898 110-139.
899 Gardner, T.N., Elliott, J.C., Sklar, Z., Briggs, G.A.D., 1992. Acoustic microscope study of the
900 elastic properties of fluorapatite and hydroxyapatite, tooth enamel and bone. Journal of
901 biomechanics, 25(11), 1265-1277.

902 Gariboldi, K., Gioncada, A., Bosio, G., Malinverno, E., Di Celma, C., Tinelli, C., Cantalamessa, G.,
903 Landini, W., Urbina, M., Bianucci, G., 2015. The dolomite nodules enclosing fossil marine
904 vertebrates in the East Pisco Basin, Peru: field and petrographic insights into the Lagerst¨atte
905 formation. Palaeogeogr. Palaeoclimatol. Palaeoecol. 438, 81–95.
906 https://doi.org/10.1016/j.palaeo.2015.07.047
907 Gariboldi, K., 2016. A note on diatom stratigraphic markers in upper Miocene sediments of the
908 Pisco Formation, Peru, and description of Delphineis urbinai sp. nov. Diatom Research, 31(3),
909 285-301.
910 Gioncada, A., Gariboldi, K., Collareta, A., Di Celma, C., Bosio, G., Malinverno, E., Lambert, O.,
911 Pike, J., Urbina, M., Bianucci, G., 2018a. Looking for the key to preservation of fossil marine
912 vertebrates in the Pisco Formation of Peru: new insights from a small dolphin skeleton. Andean
913 Geol. 45, 379–398.
914 Gioncada, A., Petrini, R., Bosio, G., Gariboldi, K., Collareta, A., Malinverno, E., Bonaccorsi, E., Di
915 Celma, C., Pasero, M., Urbina, M., Bianucci, G., 2018b. Insights into the diagenetic environment
916 of fossil marine vertebrates of the Pisco Formation (late Miocene, Peru) from mineralogical and
917 Sr-isotope data. J. S. Am. Earth Sci. 81, 141–152. https://doi.org/10.1016/j.jsames.2017.11.014.
918 Glickman L.S., 1964. Class Chondrichthyes, Subclass Elasmobranchii. In: Fundamental of
919 Paleontology (ed. Obruchev DV), pp. 196–237. Moscow–Leningrad: Nauka SSSR.
920 Golding, M. L., McMillan, R., 2021. The impacts of diagenesis on the geochemical characteristics
921 and Color Alteration Index of conodonts. Palaeobiodiversity and palaeoenvironments, 101(3),
922 803-821.
923 Grandjean, P., Albarède, F., 1989. Ion probe measurement of rare earth elements in biogenic
924 phosphates. Geochimica et Cosmochimica Acta, 53(12), 3179-3183.
925 Grandjean, P., Cappetta, H., Michard, A., Albarede, F., 1987. The assessment of REE patterns and
926 143Nd/144Nd ratios in fish remains. Earth and Planetary Science Letters, 84(2-3), 181-196.

927 Guinot, G., Cappetta, H., 2011. Enameloid microstructure of some Cretaceous Hexanchiformes and
928 Synechodontiformes (Chondrichthyes, Neoselachii): new structures and systematic implications.
929 Microscopy Research and Technique, 74(2), 196-205.
930 Harrell Jr T.L., Pérez-Huerta A., Phillips G., 2016. Strontium isotope age-dating of fossil shark
931 tooth enameloid from the Upper Cretaceous Strata of Alabama and Mississippi, USA.
932 Cretaceous Research, 62: 1-12.
933 Hampel, A., 2002. The migration history of the Nazca Ridge along the Peruvian active margin: a re-
934 evaluation and some geological implications. Earth Planet Sci. Lett., 203, 665–679.
935 Hättig, K., Stevens, K., Thies, D., Schweigert, G., Mutterlose, J., 2019. Evaluation of shark tooth
936 diagenesis-screening methods and the application of their stable oxygen isotope data for
937 palaeoenvironmental reconstructions. Journal of the Geological Society, 176(3), 482-491.
938 Hoppe, K.A., Koch, P.L., Furutani, T.T., 2003. Assessing the preservation of biogenic strontium in
939 fossil bones and tooth enamel. International Journal of Osteoarchaeology, 13(1-2), 20-28.
940 Hsu, J.T., 1992. Quaternary uplift of the Peruvian coast related to the subduction of the Nazca
941 Ridge: 13.5 to 15.6 degrees South latitude. Quat. Int. 15/16, 87–97. https://doi.org/10.1016/1040-
942 6182(92)90038-4
943 Ibaraki, M., 1993. Eocene to Early Miocene Planktonic Foraminifera from the South of Paracas,
944 Central Peru. Reports of the Faculty of Science, Shizuoka University, 27, pp. 77–93.
945 Jambura, P.L., Pfaff, C., Underwood, C.J., Ward, D.J., Kriwet, J., 2018. Tooth mineralization and
946 histology patterns in extinct and extant snaggletooth sharks, *Hemipristis* (Carcharhiniformes,
947 Hemigaleidae) - Evolutionary significance or ecological adaptation?. PLoS One, 13(8),
948 e0200951.
949 Jambura, P. L., Türtscher, J., Kindlimann, R., Metscher, B., Pfaff, C., Stumpf, S., Weber, G.W.,
950 Kriwet, J., 2020. Evolutionary trajectories of tooth histology patterns in modern sharks
951 (Chondrichthyes, Elasmobranchii). Journal of anatomy, 236(5), 753-771.

952 Jans M.M.E., 2008. Microbial bioerosion of bone–a review. In: Wisshak M, Tapanila L, editors.
953 Current developments in bioerosion. Heidelberg: Springer, 397–413.
954 John J., Seidemann, D.E., Chamberlain, J.A. Jr, Cheng, Z., Becker, M.A., 2013. Trace and minor
955 element chemistry of modern shark teeth and implications for shark tooth geochronology. In:
956 Way, M., Guan Gong, X. (Eds.), Strontium. Nova Science Publishers, 2, 27-53.
957 Jollie, M., 1962. Chordate morphology. Reinhold, New York.
958 Kemp, N.E., 1999. Integumentary system and teeth. Sharks, skates, and rays. The biology of
959 elasmobranch fish, 43-68.
960 Klein, G.D., Zúñiga y Rivero, F.G., Hay-Roe, H., Alvarez-Calderon, E., 2011. A reappraisal of the
961 Mesozoic/Cenozoic tectonics and sedimentary basins of Peru. AAPG Search and Discovery,
962 10332.
963 Kočí, T., Bosio, G., Collareta, A., Sanfilippo, R., Ekrt, B., Urbina, M., Malinverno, E., 2021. First
964 report on the cirratulid (Annelida, Polychaeta) reefs from the Miocene Chilcatay and Pisco
965 Formations (East Pisco Basin, Peru). Journal of South American Earth Sciences, 103042.
966 https://doi.org/10.1016/j.jsames.2020.103042
967 Kocsis, L., Vennemann, T.W., Ulianov, A., Brunnschweiler, J.M., 2015. Characterizing the bull
968 shark *Carcharhinus leucas* habitat in Fiji by the chemical and isotopic compositions of their
969 teeth. Environmental Biology of Fishes, 98(6), 1609-1622.
970 Kohn, M.J., Schoeninger, M.J., Barker, W.W., 1999. Altered states: effects of diagenesis on fossil
971 tooth chemistry. Geochimica et cosmochimica acta, 63(18), 2737-2747.
972 Koizumi, I., 1992. Diatomaceous sediments along the Pacific coastal areas of South America and
973 their evaluation. Journal of the Faculty of Science, Hokkaido University, Ser. IV, 23(2), 227–
974 245.
975 Lambert O., Bianucci G., Urbina M., 2014. Huaridelphis raimondii, a new early Miocene
976 Squalodelphinidae (Cetacea, odontoceti) from the Chilcatay Formation, Peru. Journal of
977 Vertebrate Paleontology, 34 (5): 987-1004.

978 Lambert O., Muizon C. de, Bianucci G., 2015. A new archaic homodont toothed cetacean
979 (Mammalia, Cetacea, Odontoceti) from the early Miocene of Peru. Geodiversitas, 37(1), 79-108.
980 Lambert, O., Muizon, C. de, Malinverno, E., Celma, C. D., Urbina, M., Bianucci, G., 2018. A new
981 odontocete (toothed cetacean) from the Early Miocene of Peru expands the morphological
982 disparity of extinct heterodont dolphins. Journal of Systematic Palaeontology, 16(12), 981-1016.
983 Lambert O., Muizon C. de, Urbina M., Bianucci G., 2020. A new longirostrine sperm whale
984 (Cetacea, Physeteroidea) from the lower Miocene of the Pisco Basin (southern coast of Peru).
985 Journal of Systematic Palaeontology, 18(20), 1707-1742.
986 Lambert O., Muizon C. de, Varas-Malca R.M., Urbina M., Bianucci G., 2021. Eurhinodelphinids
987 from the early Miocene of Peru: first unambiguous records of these hyper-longirostrine dolphins
988 outside the north atlantic realm. Rivista Italiana di Paleontologia e Stratigrafia, 127(1), 17-32.
989 Landini W., Altamirano-Sierra A., Collareta A., Di Celma C., Urbina M., Bianucci G., 2017a. The
990 late Miocene elasmobranch assemblage from Cerro Colorado (Pisco Formation, Peru). Journal of
991 South American Earth Sciences, 73, 168-190.
992 Landini W., Collareta A., Di Celma C., Malinverno E., Urbina M., Bianucci G., 2019. The early
993 Miocene elasmobranch assemblage from Zamaca (Chilcatay Formation, Peru). Journal of South
994 American Earth Sciences, 91, 352-371.
995 Landini, W., Collareta, A., Pesci, F., Di Celma, C., Urbina, M., Bianucci, G., 2017b. A secondary
996 nursery area for the copper shark Carcharhinus brachyurus from the late Miocene of Peru.
997 Journal of South American Earth Sciences, 78, 164-174.
998 LeGeros, R.Z., Tung, M.S., 1983. Chemical stability of carbonate-and fluoride-containing apatites.
999 Caries Research, 17(5), 419-429.
1000 Lübke A., Enax J., Loza K., Prymak O., Gaengler P., Fabritius H.O., Raabe D., Epple M., 2015.
1001 Dental lessons from past to present: ultrastructure and composition of teeth from plesiosaurs,
1002 dinosaurs, extinct and recent sharks. RSC Advances, 5 (76), 61612-61622.

1003 Macharé, J., Fourtanier, E., 1987. Datations des formations tertiaires du bassin de Pisco (Pérou) à
1004 partir d'associations de diatomées. Comptes rendus de l'Académie des sicences, Série 2,
1005 Mécanique, Physique, Chimie, Sciences de l'univers, Sciences de la Terre, 305(5), 407–412.
1006 Macharé J., Ortlieb L. 1992. Plio-Quaternary vertical motions and the subduction of the Nazca
1007 Ridge, central coast of Peru. Tectonophysics, 205, 97-108.
1008 Malferrari, D., Ferretti, A., Mascia, M. T., Savioli, M., Medici, L. 2019. How much can we trust
1009 major element quantification in bioapatite investigation?. ACS omega, 4(18), 17814-17822.
1010 Malinverno, E., Bosio, G., Di Celma, C., Gariboldi, K., Gioncada, A., Pierantoni, P.P., Collareta,
1011 A., Molli, G., Bagnoli, G., Sarti, G., Urbina, M., Bianucci, G. 2021. (Bio)stratigraphic overview
1012 and paleoclimatic-paleoceanographic implications of the middle-upper Eocene deposits from the
1013 Ica River Valley (East Pisco Basin, Peru). Palaeogeography Palaeoclimatology Palaeoecology,
1014 578, 110567.
1015 Marocco R., Muizon C. de, 1988a. Los vertebrados del Neogeno de la costa sur del Perú: ambiente
1016 sedimentario y condiciones de fosilización. Bulletin de l'Institut Français d'études Andines, 17,
1017 105-117.
1018 Marocco, R., Muizon, C de 1988b. Le Bassin Pisco, bassin cénozoïque d'avant arc de la côte du
1019 Pérou central: Analyse géodynamique de son remplissage. Géodynamique, 3(1-2), 3-19.
1020 Martin E.E., Scher H.D. 2004. Preservation of seawater Sr and Nd isotopes in fossil fish teeth: bad
1021 news and good news. Earth and Planetary Science Letters, 220 (1-2), 25-39.
1022 Marty, R., 1989. Stratigraphy and chemical sedimentology of Cenozoic biogenic sediments from
1023 the Pisco and Sechura Basins, Peru. PhD Thesis, Houston, Texas, Rice University.
1024 McArthur, J.M., Sahami, A.R., Thirlwall, M., Hamilton, P.J., Osborn, A.O. (1990). Dating
1025 phosphogenesis with strontium isotopes. Geochimica et Cosmochimica Acta, 54(5), 1343-1351.
1026 McArthur, J.M. 1994. Recent trends in strontium isotope stratigraphy. Terra Nova, 6(4), 331-358.

McArthur J.M., Howarth R.J., Shields G.A. Zhou Y., 2020. Strontium isotope stratigraphy. In Gradstein F.M., Ogg J.G., Schmitz M.D. and Ogg G.M. (Eds.), Geologic Time Scale 2020, Elsevier, 211-238.

Mertz D., 1966. Mikropaläontologische und sedimentologische Untersuchung der Pisco Formation Südperus. Palaeontographica Abteil B, 118, 1-51.

Møller, I.J., Melsen, B., Jensen, S. J., Kirkegaard, E., 1975. A histological, chemical and X-ray diffraction study on contemporary (*Carcharias glaucus*) and fossilized (*Macrota odontaspis*) shark teeth. Archives of Oral Biology, 20(12), 797-IN10.

Moyer, J.K., Riccio, M.L., Bemis, W.E., 2015. Development and microstructure of tooth histotypes in the blue shark, *Prionace glauca* (Carcharhiniformes: Carcharhinidae) and the great white shark, Carcharodon carcharias (Lamniformes: Lamnidae). Journal of Morphology, 276(7), 797-817.

Muizon C. de, 1988. Les Vertébrés de la Formation Pisco (Pérou). Troisième partie: Les Odontocètes (Cetacea, Mammalia) du Miocène. Travaux de l'Institut Français d'Études Andines, 42, 1-244.

Nelson, B.K., DeNiro, M.J., Schoeninger, M.J., De Paolo, D.J., Hare, P.E., 1986. Effects of diagenesis on strontium, carbon, nitrogen and oxygen concentration and isotopic composition of bone. Geochimica et Cosmochimica Acta, 50(9), 1941-1949.

Nemliher, J.G., Baturin, G.N., Kallaste, T.E., Murdmaa, I.O., 2004. Transformation of hydroxyapatite of bone phosphate from the ocean bottom during fossilization. Lithology and Mineral Resources, 39(5), 468-479.

Ørvig, T., 1951. Histologic studies of Placoderms and fossil Elasmobranchs. Arkiv für Zoologie, 2: 321-454.

Peterman, Z.E., Hedge, C.E., Tourtelot, H.A., 1970. Isotopic composition of strontium in sea water throughout Phanerozoic time. Geochimica et Cosmochimica Acta, 34(1), 105-120.

1052 Peucker-Ehrenbrink, B., Fiske, G.J., 2019. A continental perspective of the seawater 87Sr/86Sr
1053 record: a review. Chemical Geology, 510, 140-165.
1054 Peyer, B., 1968. Comparative odontology. Chicago, IL, London, The University of Chicago Press.
1055 Pfretzschner, H.U., 2001a. Pyrite in fossil bone. Neues Jahrbuch für Geologie und Paläontologie-
1056 Abhandlungen, 1-23.
1057 Pfretzschner, H.U., 2001b. Iron oxides in fossil bone. Neues Jahrbuch für Geologie und
1058 Paläontologie-Abhandlungen, 417-429.
1059 Piga, G., Santos-Cubedo, A., Brunetti, A., Piccinini, M., Malgosa, A., Napolitano, E., Enzo, S.,
1060 2011. A multi-technique approach by XRD, XRF, FT-IR to characterize the diagenesis of
1061 dinosaur bones from Spain. Palaeogeography, Palaeoclimatology, Palaeoecology, 310(1-2), 92-
1062 107.
1063 Posner, A.S., Blumenthal, N.C., Betts, F., 1984. Chemistry and structure of precipitated
1064 hydroxyapatites. In: Phosphate minerals. Springer, Berlin, Heidelberg, 330-350.
1065 Radinsky, L., 1961. Tooth histology as a taxonomic criterion for cartilaginous fishes. Journal of
1066 Morphology, 109(1), 73-92.
1067 Reif, W.E., 1973. Morphologie und Ultrastruktur des Hai-‘Schmelzes’. Zoologica Scripta, 2: 231–
1068 250.
1069 Renz, M., 2009. Desert sharks. Lehigh Acres, PaleoPress, 197 pp.
1070 Roelofs, B., Barham, M., Cliff, J., Joachimski, M., Martin, L., Trinajstic, K., 2017. Assessing the
1071 fidelity of marine vertebrate microfossil δ18O signatures and their potential for palaeo-
1072 ecological and -climatic reconstructions. Palaeogeography, Palaeoclimatology, Palaeoecology,
1073 465, 79-92.
1074 Romero, D., Valencia, K., Alarcón, P., Peña, D., Ramos, V.A., 2013. The offshore basement of
1075 Perú: Evidence for different igneous and metamorphic domains in the forearc. Journal of South
1076 American Earth Sciences, 42, 47-60.

1077 Sanfilippo, R., Kočí, T., Bosio, G., Collareta, A., Ekrt, B., Malinverno, E., Di Celma, C., Urbina,
1078 M., Bianucci, G., 2021. An investigation of vermetid reefs from the Miocene of Peru, with the
1079 description of a new species. Journal of South American Earth Sciences, 108, 103233.
1080 Schmitz, B., Åberg, G., Werdelin, L., Forey, P., Bendix-Almgreen, S.E., 1991. 87Sr/86Sr, Na, F,
1081 Sr, and La in skeletal fish debris as a measure of the paleosalinity of fossil-fish habitats.
1082 Geological Society of America Bulletin, 103(6), 786-794.
1083 Schmitz B., Ingram S.L., Dockery III D.T., Åberg G., 1997. Testing 87Sr/86Sr as a paleosalinity
1084 indicator on mixed marine, brackish-water and terrestrial vertebrate skeletal apatite in late
1085 Paleocene-early Eocene near-coastal sediments, Mississippi. Chemical Geology, 140 (3-4), 275-
1086 287.
1087 Schnetz, L., Pfaff, C., Kriwet, J., 2016. Tooth development and histology patterns in lamniform
1088 sharks (Elasmobranchii, Lamniformes) revisited. Journal of Morphology, 277(12), 1584-1598.
1089 Schrader, H., Ronning, P., 1988. Diatom biostratigraphy and coastal upwelling interpretation. In:
1090 Dunbar, R. B., Baker, P.A. (Eds.), Cenozoic Geology of the Pisco Basin. IGCP no. 156,
1091 Guidebook to Field Workshop, Lima, 135–140.
1092 Shimada K., Chandler R.E., Lam O.L.T., Tanaka T., Ward D.J., 2017. A new elusive otodontid
1093 shark (Lamniformes: Otodontidae) from the lower Miocene, and comments on the taxonomy of
1094 otodontid genera, including the 'megatoothed' clade. Historical Biology, 29 (5), 704-714.
1095 Smith, M.M., Sansom, I.J., 2000. Evolutionary origins of dentine in the fossil record of early
1096 vertebrates: diversity, development and function. Cambridge, Cambridge University Press, 65.
1097 Staudigel H., Doyle P. Zindler A. (1985). Sr and Nd isotope systematics in fish teeth. Earth and
1098 Planetary Science Letters, 76 (1-2): 45-56.
1099 Stucchi, M., Varas-Malca, R.M., Urbina-Schmitt, M., 2015. New Miocene sulid birds from Peru
1100 and considerations on their Neogene fossil record in the Eastern Pacific Ocean. Acta
1101 Palaeontologica Polonica, 61(2), 417-427.

1102 Thomasset, J.J., 1930. Recherches sur les tissus dentaires des poissons fossiles. Archives
1103 d'Anatomie Microscopique, 11, 6–153.
1104 Thornburg, T.M., Kulm, L.D., 1981. Sedimentary basins of the Peru continental margin: Structure,
1105 stratigraphy, and Cenozoic tectonics from 6 S to 16 S latitude. Nazca plate: Crustal formation
1106 and Andean convergence, 154, 393-422.
1107 Travis, R.B., Gonzales, G., Pardo, A., 1976. Hydrocarbon potential of coastal basins of Peru. In:
1108 Halbouty, M.T., and others (Eds.), Circum- Pacific energy and mineral resources. Tulsa,
1109 American Association of Petroleum Geologists Memoir, 25, 331-338.
1110 Tsuchi, R., Shuto, T., Takayama, T., Fujiyoshi, A, Koizumi, I., Ibaraki, M., Rangel, Z.C., Aldana,
1111 A.M., 1988. Fundamental Data on Cenozoic Biostratigraphy of the Pacific Coast of Peru. In:
1112 Tsuchi R. (Ed.), Report of Andean studies. Shizuoka University, Special volume 3, 45–70.
1113 Tütken, T., Vennemann, T.W., Pfretzschner, H.U., 2008. Early diagenesis of bone and tooth apatite
1114 in fluvial and marine settings: constraints from combined oxygen isotope, nitrogen and REE
1115 analysis. Palaeogeography, Palaeoclimatology, Palaeoecology, 266(3-4), 254-268.
1116 Tütken, T., Vennemann, T.W., Pfretzschner, H.U., 2011. Nd and Sr isotope compositions in modern
1117 and fossil bones–Proxies for vertebrate provenance and taphonomy. Geochimica et
1118 Cosmochimica Acta, 75(20), 5951-5970.
1119 Tütken, T., Weber, M., Zohar, I., Helmy, H., Bourgon, N., Lernau, O., Jochum, K.P., Sisma-
1120 Ventura, G., 2020. Strontium and oxygen isotope analyses reveal Late Cretaceous shark teeth in
1121 Iron Age strata in the Southern Levant. Frontiers in Ecology and Evolution, 423.
1122 Tucker, A.S., Fraser, G.J., 2014. Evolution and developmental diversity of tooth regeneration.
1123 Seminars in Cell & Developmental Biology, 25–26, 71–80.
1124 Uhen, M.D., Pyenson, N.D., Devries, T.J., Urbina, M., Renne, P.R., 2011. New middle Eocene
1125 whales from the Pisco Basin of Peru. J. Paleontol., 85, 955–969.
1126 Ullmann, C.V., Korte, C., 2015. Diagenetic alteration in low-Mg calcite from macrofossils: a
1127 review. Geol. Q., 59, 3–20.

1128 Veizer, J., 1989. Strontium isotopes in seawater through time. Annual Review of Earth and
1129 Planetary Sciences, 17(1), 141-167.
1130 Veizer, J., Buhl, D., Diener, A., Ebneth, S., Podlaha, O.G., Bruckschen, P., Jasper, T., Korte, C.,
1131 Schaaf, M., Ala, D., Azmy, K., 1997. Strontium isotope stratigraphy: potential resolution and
1132 event correlation. Palaeogeography, Palaeoclimatology, Palaeoecology, 132(1-4), 65-77.
1133 Vennemann, T.W., Hegner, E., 1998. Oxygen, strontium, and neodymium isotope composition of
1134 fossil shark teeth as a proxy for the palaeoceanography and palaeoclimatology of the Miocene
1135 northern Alpine Paratethys. Palaeogeography, Palaeoclimatology, Palaeoecology, 142(3-4), 107-
1136 121.
1137 Vennemann, T.W., Hegner, E., Cliff, G., Benz, G.W., 2001. Isotopic composition of recent shark
1138 teeth as a proxy for environmental conditions. Geochimica et Cosmochimica Acta, 65(10), 1583-
1139 1599.
1140 von Huene, R., Pecher, I.A., Gutscher, M.A., 1996. Development of the accretionary prism along
1141 Peru and material flux after subduction of Nazca Ridge. Tectonics, 15(1), 19-33.
1142 Wickman, F.E., 1948. Isotope ratios: a clue to the age of certain marine sediments. The Journal of
1143 Geology, 56(1), 61-66.
1144 Wilmers, J., Waldron, M., Bargmann, S., 2021. Hierarchical Microstructure of Tooth Enameloid in
1145 Two Lamniform Shark Species, Carcharias taurus and Isurus oxyrinchus. Nanomaterials, 11(4),
1146 969.
1147 Wood R.C., Johnson-Gove J., Gaffney E.S., Maley K.F., 1996. Evolution and phylogeny of
1148 leatherback turtles (Dermochelyidae), with descriptions of new fossil taxa. Chelonian
1149 Conservation and Biology, 2, 266-86.
1150 Zazzo, A., Lécuyer, C., Sheppard, S.M., Grandjean, P., Mariotti, A., 2004. Diagenesis and the
1151 reconstruction of paleoenvironments: a method to restore original δ18O values of carbonate and
1152 phosphate from fossil tooth enamel. Geochimica et Cosmochimica Acta, 68(10), 2245-2258.
1153

Figure captions

Figure 1. Schematic sections of osteodont and orthodont shark teeth showing tooth histology and microstructure. *Cosmopolitodus hastalis* from Zamaca is shown as an example for the osteodont histotype; *Physogaleus contortus* from south of Cerro Colorado is shown as an example for the orthodont histotype.

Figure 2. A. Satellite image of the localities south of Cerro Colorado (14°23'46.8'' S, 75°53'15.8'' W; and 14°23'01.9'' S, 75°53'58.8'' W), Zamaca (14°37'40.0'' S, 75°38'45.0'' W), and Media Luna (14°33'50.0'' S, 75°54'00.0'' W) (yellow stars) along the western side of the Ica River (Ica Desert). Based on Google Earth image. At the top right corner, the map indicates the major structural highs that define the major Cenozoic sedimentary basins along the Peruvian coast. **B.** Stratigraphic scheme of the East Pisco Basin fill along the Ica River with the stratigraphic position of the volcanic ash layers dated with $^{40}Ar/^{39}Ar$ method in the Chilcatay Formation. Redrawn after Di Celma et al. (2019).**Figure 3.** Field photos and stratigraphic section. **A.** Field photo of the shark tooth-bearing bed ShB-4 at the base of the Ct2 sequence at the Zamaca locality. Note the abrupt change from the light-grey siltstones of Ct1a to the brownish coarse-grained sandstones found at the base of Ct2. Note also the burrowed firmground surface (CE0.2) at the base of Ct2, with large *Thalassinoides* and *Gyrolithes* defining a *Glossifungites* ichnofacies (30-cm-long hammer for scale). The red arrow indicates the sampled horizon. **B.** Stratigraphic section measured at the Zamaca locality showing the stratigraphic position of the four shark tooth-bearing intervals, including the "ShB-4" discussed in the present paper. After Landini et al. (2019). **C.** Tooth of *Carcharocles chubutensis* from the tooth-bearing bed ShB-4 at Zamaca. **D.** Specimen of *Sphyrna zygaena* from the tooth-bearing bed ShB-4 at Zamaca. **E.** Field photo of the sampling site south of Cerro Colorado, where the eurhinodelphinid-like odontocete skeleton has been found. The red arrow indicates the approximate position of the sampled horizon. **F.** Field photo of the sampling site at Media Luna. The red arrow indicates the approximate position of the sampled horizon, named "Terrace 1".

Figure 4. Overview of the main shark taxa analyzed in the present study, with photos of some studied tooth samples and silhouettes to suggest the body shapes.

Figure 5. Shark tooth microstructural image. **A.** Thin section slides of two lamniform shark teeth (*Megalolamna paradoxodon* and *Cosmopolitodus hastalis*) from Media Luna and Zamaca, built from composite photomicrographs obtained under transmitted plane-polarized light. **B.** Photomicrograph of a tooth cusp of *C. hastalis* collected at the eurhinodelphinid-like odontocete locality south of Cerro Colorado under transmitted plane-polarized light, showing enameloid and osteodentine with well preserved vascular canals. **C.** Photomicrograph of a tooth cusp of *C. hastalis* from Zamaca showing enameloid and osteodentine under transmitted plane-polarized light. Note the three layers of enameloid, from outer to inner: Shiny-Layered Enameloid (SLE); Parallel-Bundled Enameloid (PBE); and Tangle-Bundled Enameloid (TBE). **D.** Back-scattered electron (BSE) image of the tooth cusp of *M. paradoxodon* from Media Luna showing the enameloid, the dentine-enameloid junction, and the osteodentine. **E.** Photomicrograph showing the enameloid and the osteodentine of a *C. hastalis* tooth from Zamaca under transmitted cross-polarized light. Note the three layer of enameloid, from outer to inner: Shiny-Layered Enameloid (SLE); Parallel-Bundled Enameloid (PBE); and Tangle-Bundled Enameloid (TBE). **F.** Photomicrograph of a tooth of *Physogaleus contortus* (close-up) collected at the eurhinodelphinid-like odontocete locality south of Cerro Colorado, showing enameloid and orthodentine under transmitted plane-polarized light. **G.** Photomicrograph of a tooth root of *C. hastalis* collected at the eurhinodelphinid-like odontocete locality south of Cerro Colorado under transmitted plane-polarized light, showing the osteodentine resembling the bone tissue. **H.** Back-scattered electron (BSE) image of a tooth root of *C. hastalis* collected at the eurhinodelphinid-like odontocete locality south of Cerro Colorado, showing the osteodentine resembling the bone tissue, with dentinal tubules. DEJ = dentine-enameloid junction; DT = dentinal tubules; EN = enameloid; OD = osteodentine; OR = orthodentine; PBE = Parallel-Bundled Enameloid; SLE = Shiny-Layered Enameloid; TBE = Tangle-Bundled Enameloid; VC = vascular canals.

Figure 6. Shark tooth microstructures. **A.** Secondary electron (SE) image of crystallite bundles forming the enameloid of a *Megalolamna paradoxodon* tooth from Media Luna. **B.** Secondary electron (SE) image (close-up) of differently oriented crystallite bundles forming the enameloid of a *Cosmopolitodus hastalis* tooth collected at the eurhinodelphinid-like odontocete locality south of Cerro Colorado. **C.** Secondary electron (SE) image of the osteodentine of a *C. hastalis* tooth collected at the eurhinodelphinid-like odontocete locality south of Cerro Colorado, showing randomly disposed microscopic crystalline artefacts that probably formed during diagenesis. **D.** Secondary electron (SE) image close-up of the osteodentine from the same tooth as Figure 8D, showing randomly disposed microscopic crystalline artefacts probably from diagenesis. **E.** Back-scattered electron (BSE) image of the root of a *M. paradoxodon* from Media Luna, showing microborings affecting the osteodentine. **F.** Secondary electron (SE) image (close-up) of a microboring in Figure 8E exhibiting a Fe-oxide framboidal spherule, i.e. the ghost of a pyrite framboid. **G.** Back-scattered electron (BSE) image of a close-up of microborings in Figure 8E, showing an infill of apatite material and Fe-oxide framboidal spherules. Note the brighter hypermineralized rim that demonstrates the bacterial origin of the microborings (Jans, 2008). **H.** Compositional EDS mapping of Figure 8G, showing the Fe distribution within the microborings, highlighting the presence of Fe-oxides that are interpreted as relicts of framboidal pyrite.

Figure 7. Compositional images of shark teeth. **A.** Back-scattered electron (BSE) image of the outer tooth layers of a *Cosmopolitodus hastalis* collected at the eurhinodelphinid-like odontocete locality south of Cerro Colorado, showing the enameloid, the dentine-enameloid junction and the osteodentine. **B.** Compositional EDS map, showing the S distribution in the enameloid, dentine-enameloid junction and osteodentine. **C.** Back-scattered electron (BSE) image (close-up) of the dentine-enameloid junction of a *Megalolamna paradoxodon* from Media Luna, showing the enameloid, the dentine-enameloid junction and the osteodentine. **D.** Compositional EDS map, showing the P, Ca and S distributions in the enameloid, dentine-enameloid junction, and osteodentine. **E.** Compositional EDS map, showing the Na distribution in the enameloid, dentine-

enameloid junction and osteodentine. **F.** Compositional EDS map, showing the Cl distribution in the enameloid, dentine-enameloid junction and osteodentine. **G.** Back-scattered electron (BSE) image of the osteodentine near the dentine-enameloid junction of a *M. paradoxodon* from Media Luna, resembling a compact bone structure and showing dentinal tubules wrapped into a fibrous meshwork. **H.** Compositional EDS map, showing P, Ca and S distributions in the fibrous meshwork and osteodentine. DEJ = dentine-enameloid junction; DT = dentinal tubules; EN = enameloid; FM = fibrous meshwork; OD = osteodentine.

Figure 8. Compositional images of enameloid. **A.** Back-scattered electron (BSE) image of the enameloid of a *Cosmopolitodus hastalis* tooth collected at the eurhinodelphinid-like odontocete locality south of Cerro Colorado, showing the shiny-layered enameloid. **B.** Compositional EDS map, showing the Mg distribution. **C.** Compositional EDS map, showing the F distribution. **D.** Compositional EDS map, showing the Fe distribution. PBE = Parallel-Bundled Enameloid; SLE = Shiny-Layered Enameloid.

Figure 9. Multi-component plot of $^{87}Sr/^{86}Sr$ ratio vs Sr concentration. Dark orange and light orange fields are based on the Sr content from recent and fossil shark teeth (Grandjean et al., 1987; Schmitz et al., 1991; Vennemann and Hegner, 1998; Vennemann et al., 2001; Martin and Scher, 2004; Becker et al., 2008; John et al., 2013; Kocsis et al., 2015). Ct2 = Zamaca; CC-EU = eurhinodelphinid-like odontocete locality; MDL-T1 = Media Luna; MSD = *Macrosqualodelphis ukupachai* locality.

Figure 10. Schematic chronostratigraphy of the Ct0, Ct1 and Ct2 sequences of the Chilcatay Formation at different localities of the western side of the Ica River Valley according to Strontium Isotope Stratigraphy, with satellite location map. Data at the localities of Ullujaya and Roca Negra after Bosio et al. (2020).

Table captions

Table 1. Sample list and description, with locality and stratigraphic data, and strontium isotope results reporting $^{87}Sr/^{86}Sr$ values and standard deviations, corrections based on the NIST NBS 987 and USGS EN-1 standards, and the preferred age calculated from the LOESS 6 (McArthur et al., 2020) for each sample.

Table 2. Major element chemical composition (wt %) by means of Energy-dispersive X-ray spectroscopy (EDS) of the enameloid and dentine in two selected fossil shark teeth.

Table 3. Inductively coupled plasma optical emission spectrometry (ICP-OES) results reporting Ca, Mg, Sr, Fe, and Mn content with standard deviation of the analyzed shark teeth and the two analyzed oysters.

Table 4. Sr ages for each stratigraphic level at the investigated locality, calculated from the mean $^{87}Sr/^{86}Sr$ values and using the LOESS 6 Table (McArthur et al., 2020), and showing the maximum age, the preferred age and the minimum age.

Table 5. New evaluations of the Sr ages for the P0 and Chilcatay strata by Bosio et al. (2020) re-calculated by using the LOESS 6 Table (McArthur et al., 2020).

Samples	Locality	Unit	Horizon	Description	Measured $^{87}Sr/^{86}Sr$	$\pm 2s_{mean}$	Corrected $^{87}Sr/^{86}Sr$	Preferred age LOESS 6 (Ma)
Ct2-1	Zamaca	Ct2a (base)	ShB-4	*Cosmopolitodus hastalis*, moderately well preserved	0.708555	0.000005	0.708569	18.30
Ct2-3	Zamaca	Ct2a (base)	ShB-4	*Isurus oxyrinchus*, well preserved	0.708562	0.000005	0.708576	18.20
CC-EU-1	Cerro Colorado	undifferentiated strata	Eurhinodelphinid-like odontocete	*Cosmopolitodus hastalis*, moderately well preserved	0.708512	0.000005	0.708526	18.90
CC-EU-2	Cerro Colorado	undifferentiated strata	Eurhinodelphinid-like odontocete	*Isurus oxyrinchus*, well preserved	0.708512	0.000005	0.708526	18.90
CC-EU-3	Cerro Colorado	undifferentiated strata	Eurhinodelphinid-like odontocete	*Physogaleus contortus*, well preserved	0.708516	0.000005	0.708530	18.85
MDL-T1-1	Media Luna	Ct0	Terrace 1	*Isurus* sp., moderately well preserved	0.708419	0.000005	0.708433	20.20
MDL-T1-2	Media Luna	Ct0	Terrace 1	*Isurus* sp., well preserved	0.708401	0.000005	0.708415	20.45
MDL-T1-3	Media Luna	Ct0	Terrace 1	*Isurus* sp., well preserved	0.70835	0.000005	0.708364	21.20
MDL-T1-4	Media Luna	Ct0	Terrace 1	*Isurus* sp., moderately well preserved	0.708304	0.000005	0.708318	21.95
MSD-1	South of Cerro Colorado	undifferentiated strata	*Macrosqualodelphis ukupachai*	*Cosmopolitodus hastalis*, moderately well preserved	0.708513	0.000005	0.708527	18.85
MSD-2	South of Cerro Colorado	undifferentiated strata	*Macrosqualodelphis ukupachai*	*Cosmopolitodus hastalis*, moderately well preserved	0.708518	0.000006	0.708532	18.80
MSD-OS1	South of Cerro Colorado	undifferentiated strata	*Macrosqualodelphis ukupachai*	Oyster specimen, nacre layers	0.708559	0.000005	0.708573	18.25
MSD-OS2	South of Cerro Colorado	undifferentiated strata	*Macrosqualodelphis ukupachai*	Oyster specimen, nacre layers	0.708509	0.000005	0.708523	18.90

Samples	Type	F	Na	Mg	S	Cl	Fe	Sr	CaO	P_2O_5	Sum
CC-EU-40	enameloid	2.79	-	-	-	-	-	-	55.84	43.10	101.73
CC-EU-41	enameloid	2.07	-	-	-	-	-	-	53.88	40.76	96.71
CC-EU-45	enameloid	2.46	-	-	-	-	-	-	55.39	42.16	100.01
CC-EU-47	enameloid	2.67	0.57	-	0.25	-	-	-	54.25	41.63	99.37
CC-EU-49	enameloid	2.78	0.61	-	0.26	-	-	-	52.43	40.41	96.50
MDL-T1-53	enameloid	2.95	0.52	0.08	0.16	-	-	0.54	56.75	44.19	105.19
MDL-T1-54	enameloid	2.83	0.52	0.08	-	-	-	-	54.79	42.64	100.86
CC-EU-42	dentine	1.88	0.63	-	2.11	0.10	-	-	51.69	35.36	91.76
CC-EU-43	dentine	1.94	0.56	-	2.14	0.16	-	-	47.98	33.16	85.93
CC-EU-44	dentine	1.70	0.85	-	2.03	0.19	-	-	49.31	33.97	88.05
CC-EU-46	dentine	2.02	0.75	0.28	2.00	-	-	0.42	51.50	35.67	92.64
CC-EU-48	dentine	2.51	0.56	0.27	2.18	-	-	0.42	49.09	33.80	88.82
CC-EU-50	dentine	1.55	0.47	0.28	1.89	0.22	-	0.47	48.26	32.84	85.99
MDL-T1-51	dentine	1.59	1.15	0.23	2.05	0.81	0.14	0.53	47.97	33.41	87.88
MDL-T1-52	dentine	1.51	1.15	0.12	2.08	0.79	0.15	0.31	50.02	34.42	90.55

Samples	Ca (ppm)	± s	Mg (ppm)	± s	Sr (ppm)	± s	Fe (ppm)	± s	Mn (ppm)	± s
Ct2-1	323200	2361	1445	9	1674.0	4.9	1842.0	7.5	83.9	0.2
Ct2-3	370030	4438	982	2	2326.0	6.2	901.6	2.7	95.4	0.4
CC-EU-1	364020	3960	1292	2	2299.0	5.6	770.4	6.5	154.0	0.9
CC-EU-2	368560	2965	1033	8	2240.0	10.4	1266.0	7.6	208.0	1.0
CC-EU-3	372500	2092	1708	9	1901.0	9.2	715.5	2.7	128.0	0.5
MDL-T1-1	362430	1933	914	4	2278.0	9.5	997.1	4.5	87.8	0.3
MDL-T1-2	372440	2837	936	5	2254.0	13.5	1579.0	8.3	70.4	0.2
MDL-T1-3	368650	2510	1025	8	2310.0	9.2	1937.0	9.1	54.2	0.2
MDL-T1-4	363070	2227	793	4	1926.0	11.3	2295.0	8.3	200.0	1.1
MSD-1	369820	2670	900	5	2323.0	6.5	1188.0	4.3	224.0	0.8
MSD-2	364480	2843	963	12	2117.0	16.4	1253.0	8.6	188.0	1.5
MSD-OS1	392500	3979	2074	10	590.7	3.3	68.5	0.6	315.0	1.3
MSD-OS2	390530	1405	3248	12	532.6	2.5	214.0	1.1	476.0	2.0

Stratigraphic level	minus 2 s.e.	$^{87}Sr/^{86}Sr$ mean value	plus 2 s.e.	Maximum age (Ma)	Preferred age (Ma)	Minimum age (Ma)
ShB-4, Zamaca, Ct2a base	0.708566	0.708573	0.708580	18.4	**18.25**	18.1
Eurhinodelphinid-like odontocete, S of Cerro Colorado, undifferentiated	0.708525	0.708528	0.708530	18.9	**18.85**	18.8
Terrace 1, Media Luna, Ct0	0.708331	0.708383	0.708435	21.8	**20.90**	20.1
Macrosqualodelphis ukupachai, S of Cerro Colorado, undifferentiated	0.708516	0.708539	0.708562	19.1	**18.70**	18.3

	Stratigraphic level	minus 2 s.e.	$^{87}Sr/^{86}Sr$ mean value	plus 2 s.e.	Maximum age (Ma)	Preferred age (Ma)	Minimum age (Ma)
P0	Lower P0	0.708799	0.708812	0.708825	14.7	**13.58**	12.6
Ct1	Key bed B	0.708530	0.708548	0.708566	18.9	**18.58**	18.3
	Key bed C	0.708536	0.708549	0.708561	18.8	**18.57**	18.4
	Mollusk- and barnacle-rich horizon	0.708528	0.708530	0.708532	18.9	**18.82**	18.5
	PN Oyster bed	0.708510	0.708532	0.708554	19.1	**18.80**	18.7

Cosmopolitodus hastalis (osteodont)

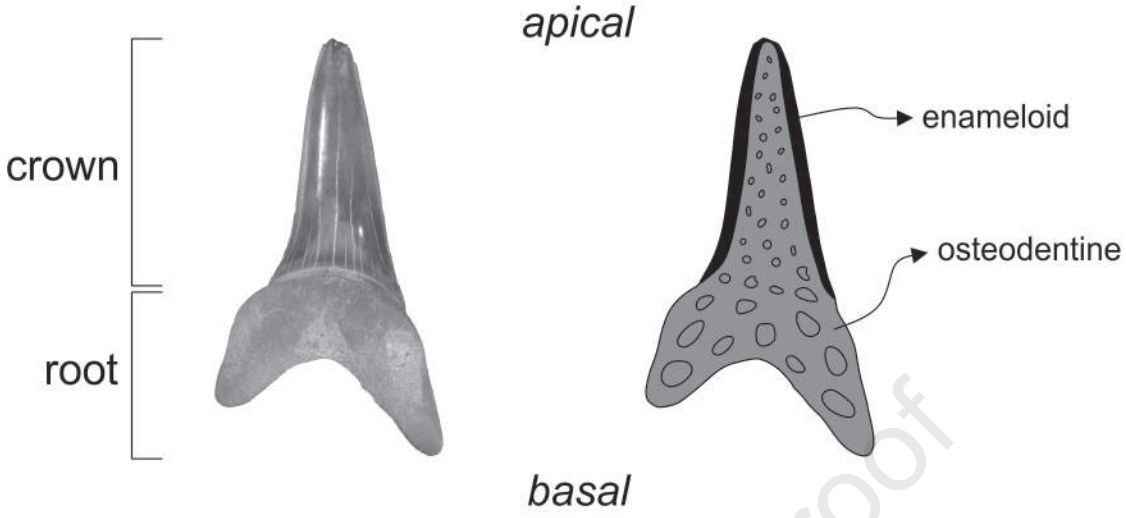

Physogaleus contortus (orthodont)

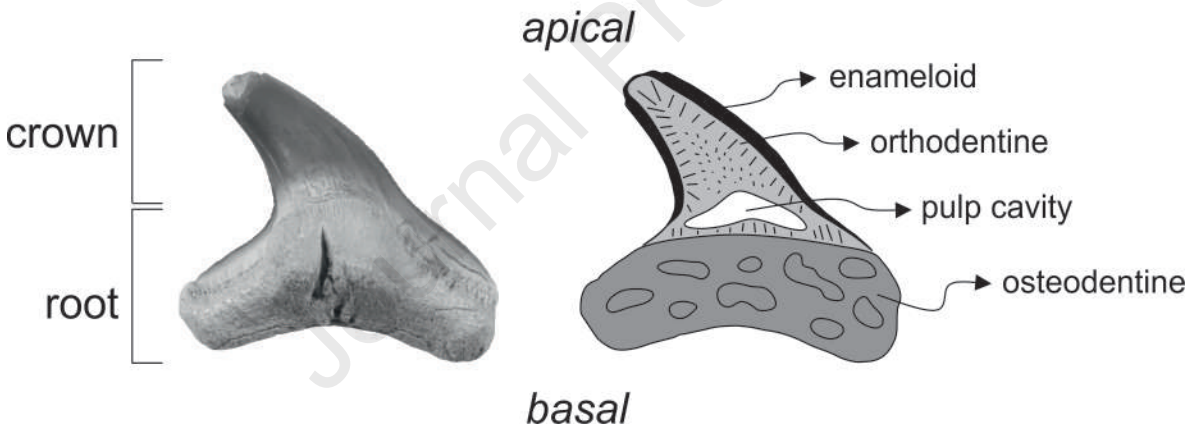

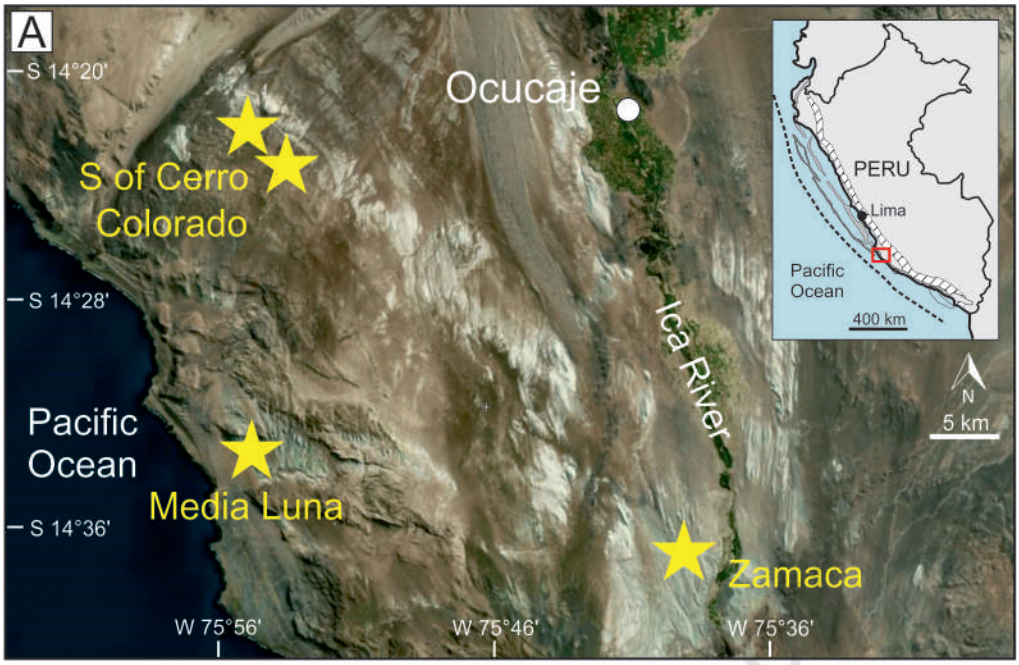
A
S 14°20'
Ocucaje
S of Cerro Colorado
S 14°28'
Pacific Ocean
Media Luna
S 14°36'
Ica River
Zamaca
W 75°56'
W 75°46'
W 75°36'
PERU
Lima
Pacific Ocean
400 km
N
5 km

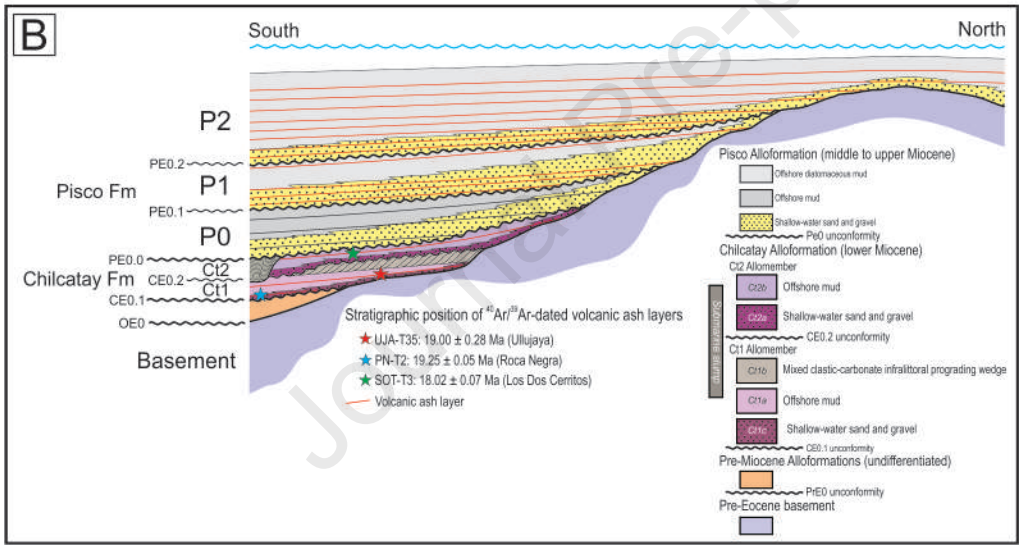
B
South
North
P2
PE0.2
Pisco Fm
P1
PE0.1
P0
PE0.0
Chilcatay Fm
CE0.2
Ct2
Ct1
CE0.1
OE0
Basement
Stratigraphic position of 40Ar/39Ar-dated volcanic ash layers
UJA-T35: 19.00 ± 0.28 Ma (Ullujaya)
PN-T2: 19.25 ± 0.05 Ma (Roca Negra)
SOT-T3: 18.02 ± 0.07 Ma (Los Dos Cerritos)
Volcanic ash layer
Pisco Alloformation (middle to upper Miocene)
Offshore diatomaceous mud
Offshore mud
Shallow-water sand and gravel
Pe0 unconformity
Chilcatay Alloformation (lower Miocene)
Ct2 Allomember
Ct2b
Offshore mud
Ct2a
Shallow-water sand and gravel
CE0.2 unconformity
Ct1 Allomember
Ct1b
Mixed clastic-carbonate infralittoral prograding wedge
Ct1a
Offshore mud
Ct1c
Shallow-water sand and gravel
CE0.1 unconformity
Pre-Miocene Alloformations (undifferentiated)
PrE0 unconformity
Pre-Eocene basement

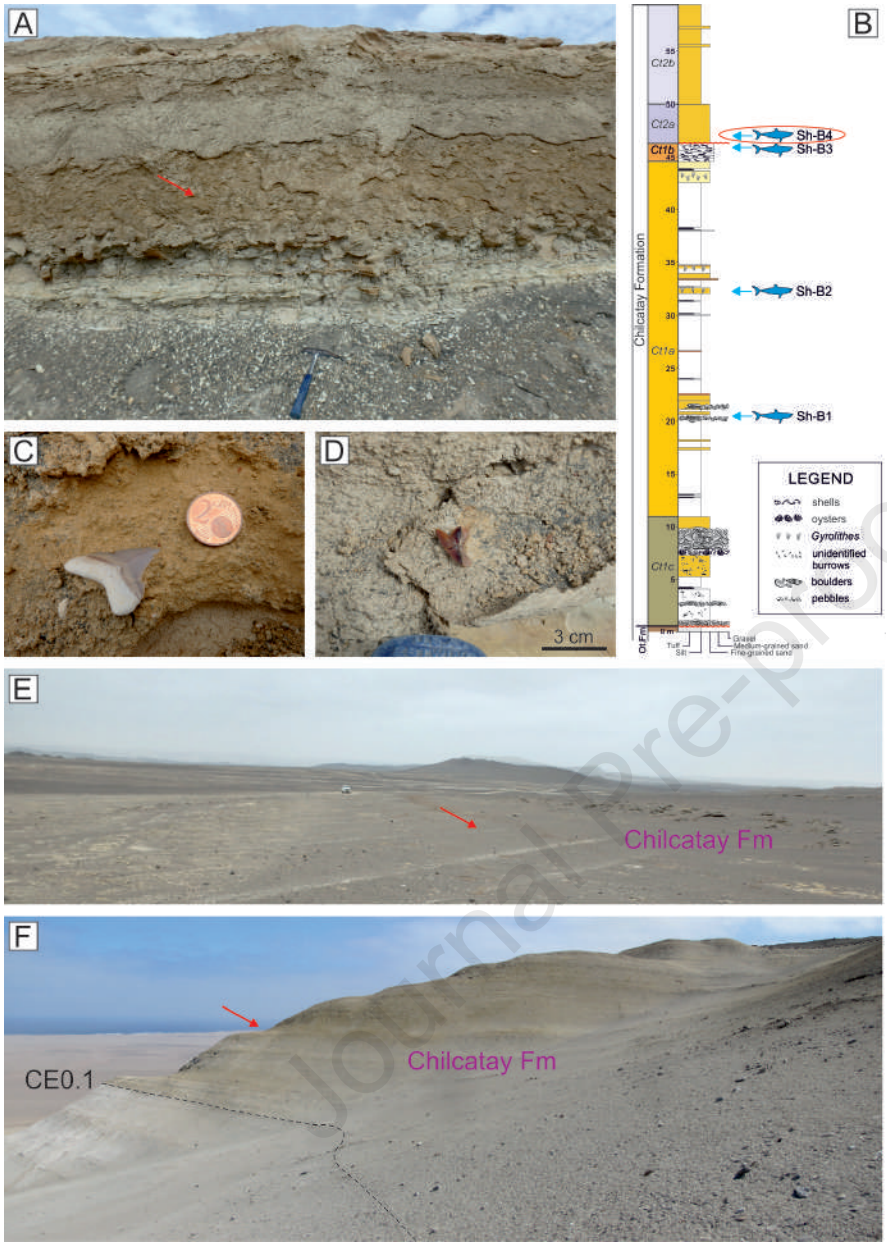

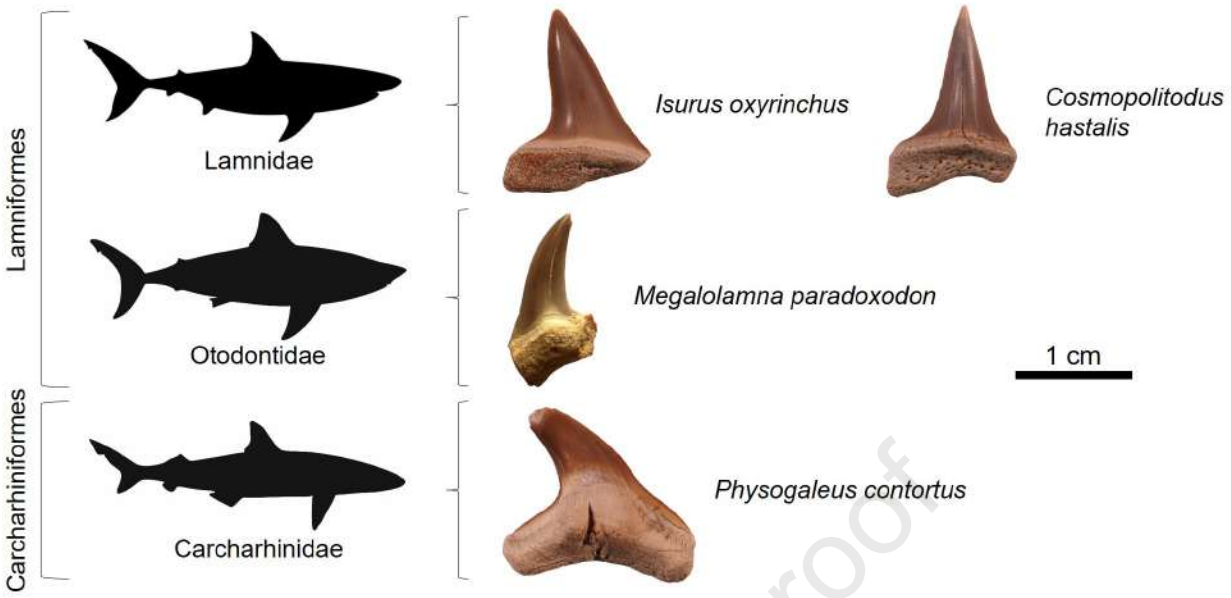

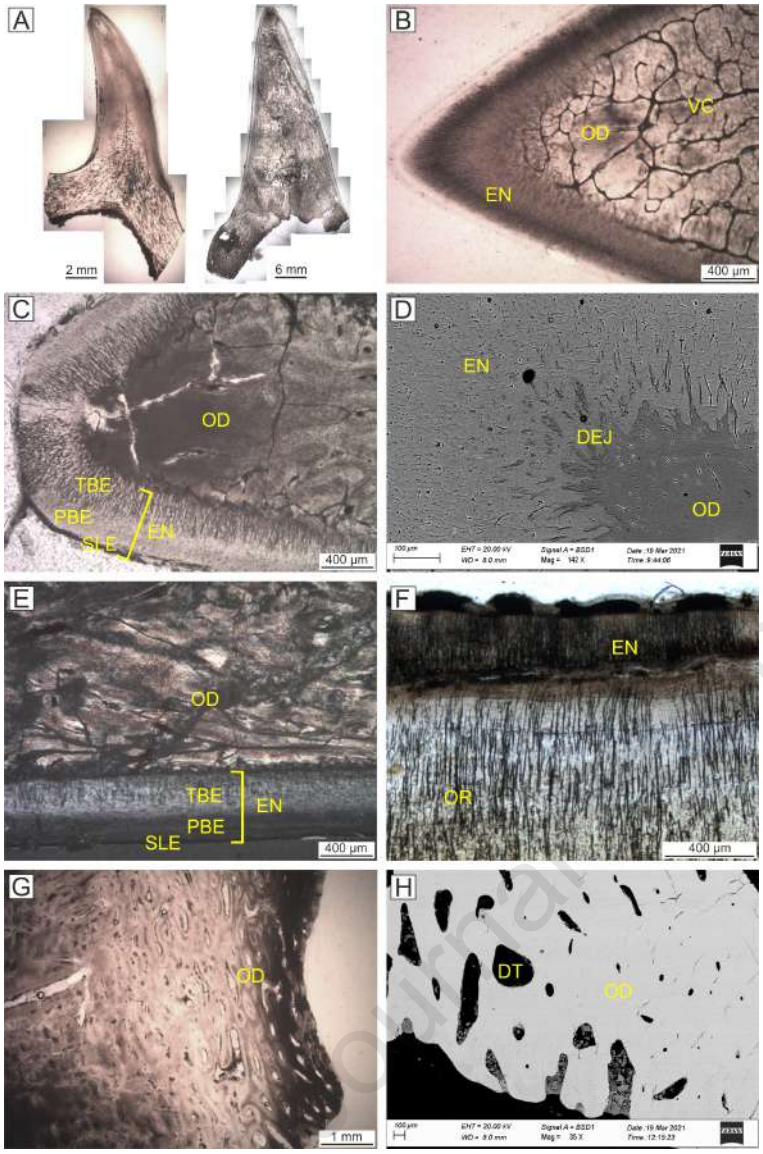

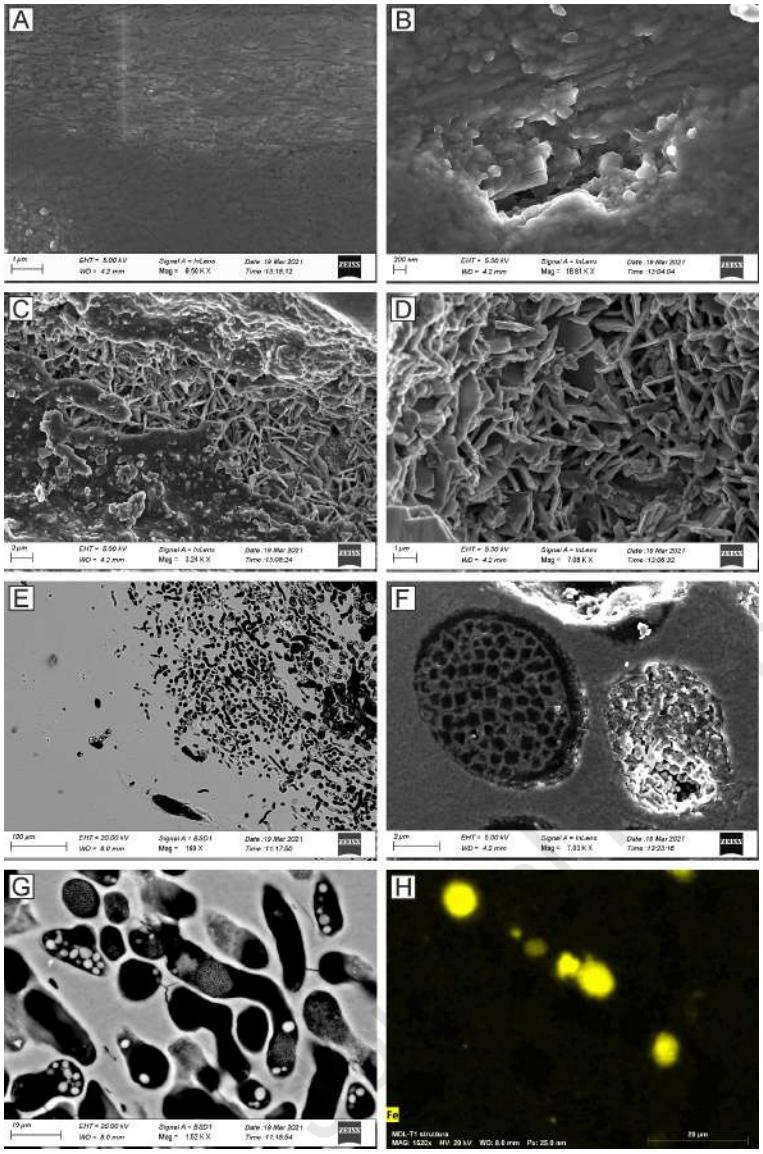

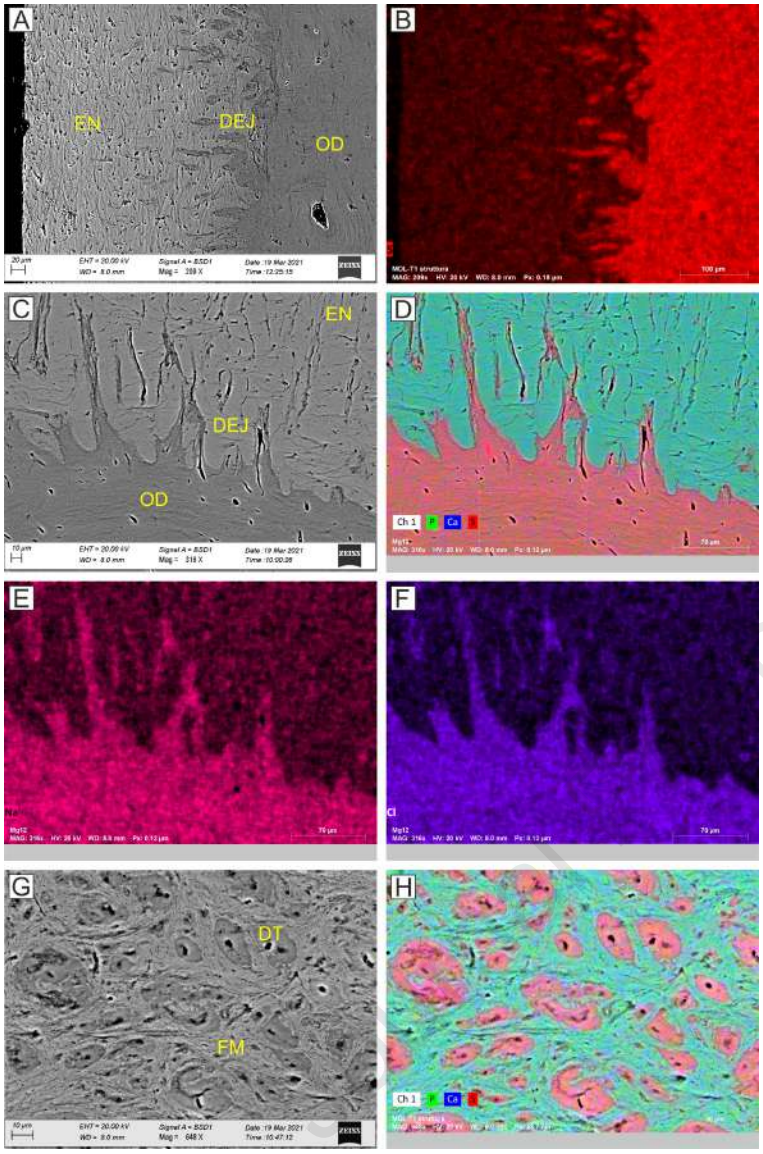

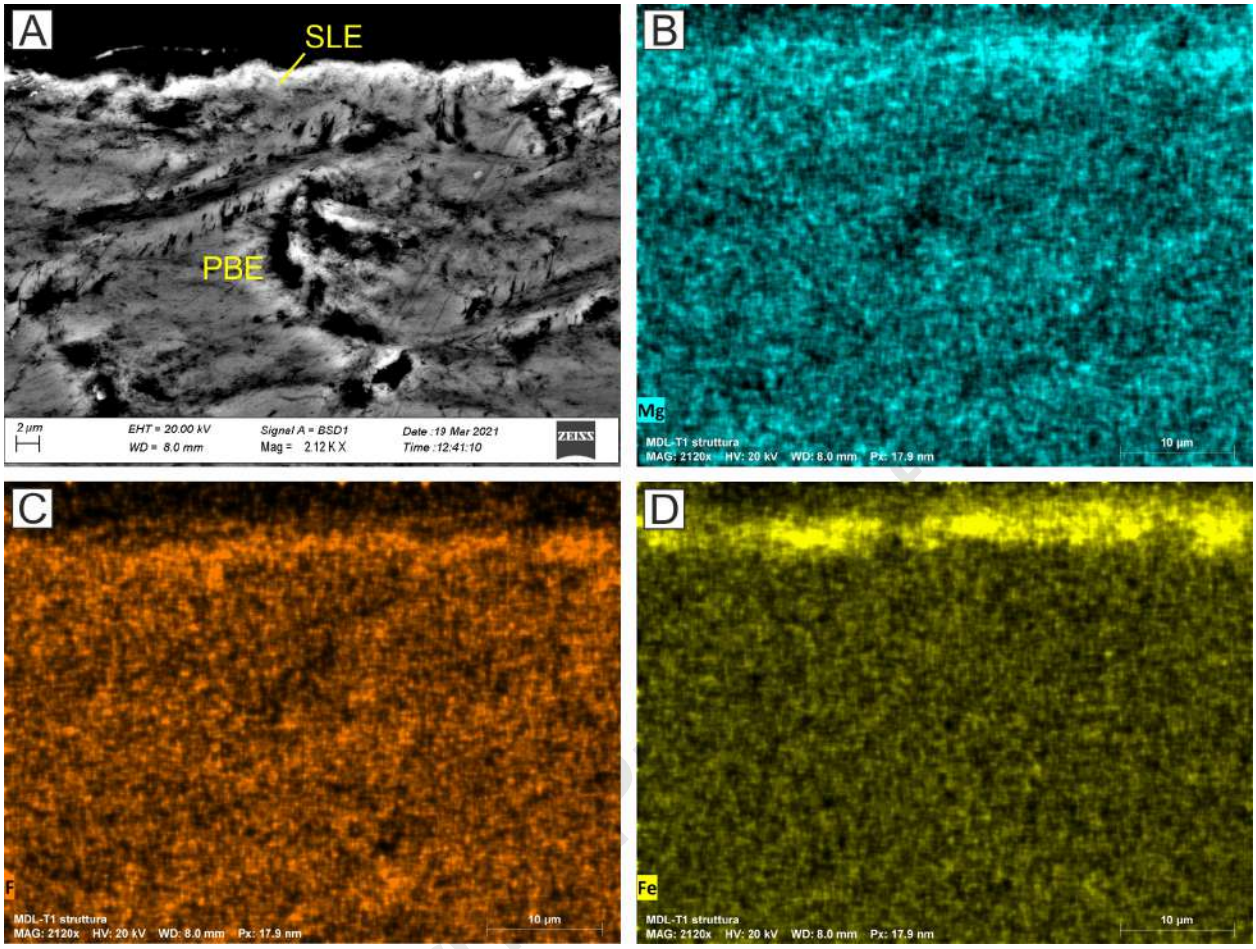

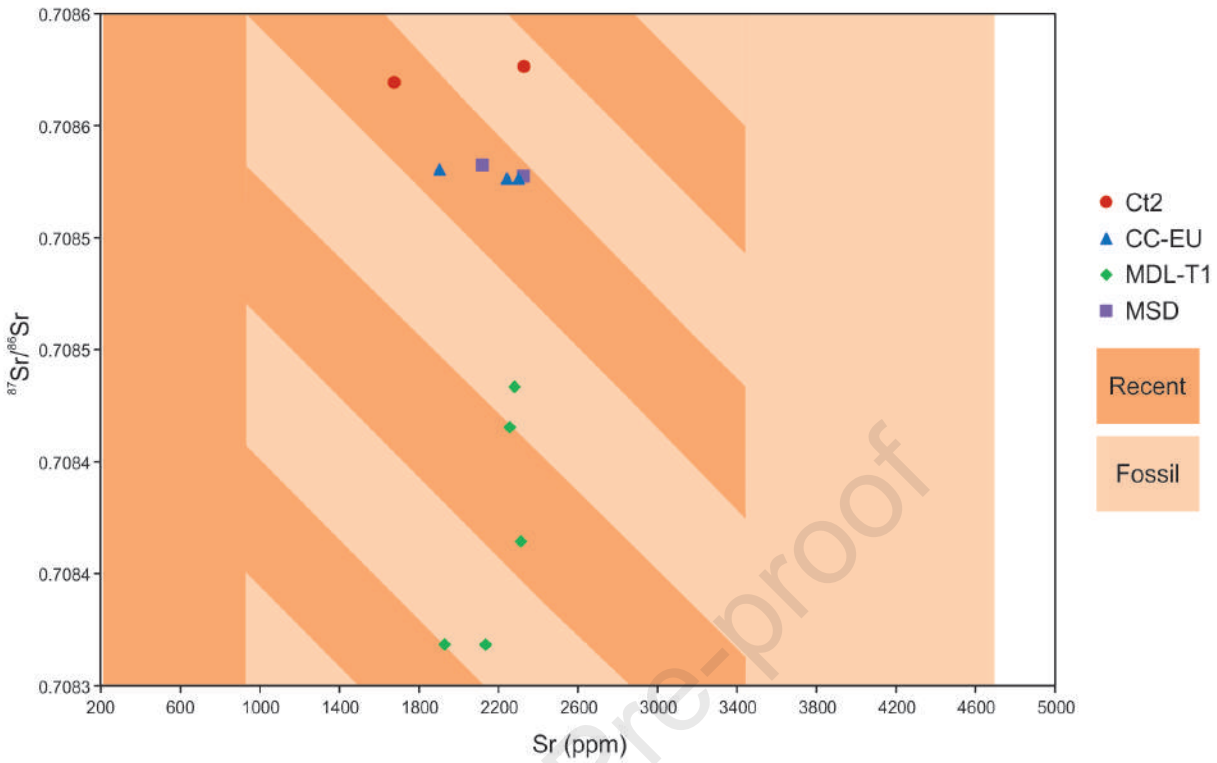

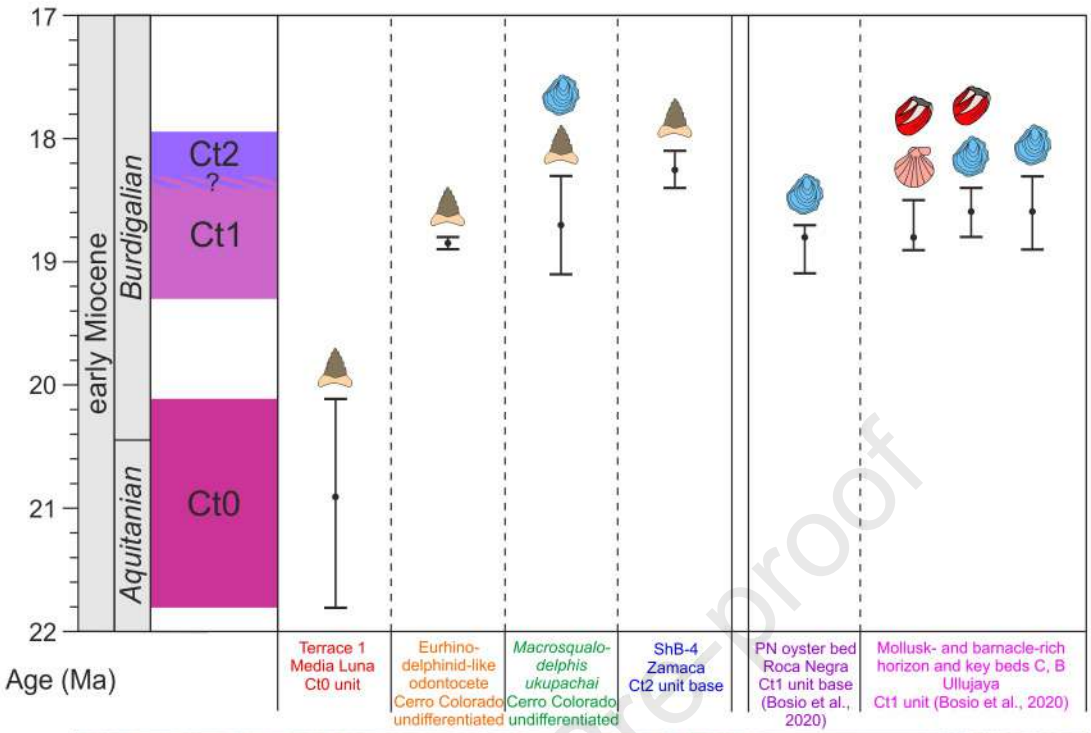

Declaration of interests

☐ The authors declare that they have no known competing financial interests or personal relationships that could have appeared to influence the work reported in this paper.

☒ The authors declare the following financial interests/personal relationships which may be considered as potential competing interests:

Giovanni Bianucci reports financial support was provided by Government of Italy Ministry of Education University and Research. Giovanni Bianucci reports financial support was provided by National Geographic Society Committee for Research Exploration grant.